공학박사 학위논문

Monte Carlo Simulations and Experiments of Metal Nanoparticle Enhanced Low-Energy Radiotherapy

금속나노입자 저에너지 방사선치료를 위한 몬테카를로 시뮬레이션과 실험

2018년 2월

서울대학교 대학원

융합과학부 방사선융합의생명 전공

성 원 모

A Disseration for the Degree Doctor of Philosophy

Monte Carlo Simulations and Experiments of Metal Nanoparticle Enhanced Low-Energy Radiotherapy

금속나노입자 저에너지 방사선치료를 위한 몬테카를로 시뮬레이션과 실험

February 2018

Wonmo Sung

Program in Biomedical Radiation Sciences

Department of Transdisciplinary Studies

Seoul National University

ABSTRACT

Monte Carlo Simulations and Experiments of Metal Nanoparticle Enhanced Low-Energy Radiotherapy

Wonmo Sung

Program in Biomedical Radiation Sciences

Department of Transdisciplinary Studies

Graduate School of Convergence Science and Technology

Seoul National University

The goal of radiation therapy is to deliver therapeutic doses to tumors while sparing surrounding normal tissue. Even though various techniques such as intensity-modulated radiation therapy (IMRT) have been introduced, increasing the therapeutic ratio is still a challenging goal in radiation cancer treatment. Over the last decade, the radiosensitizing potential of nanoparticles (NPs) has shown great promise. Interests in this field have particularly focus on gold nanoparticles (GNPs) due to its biocompatibility and high atomic number. However, macroscopic radiation dose calculations by mass energy absorption fail to predict observed experimental findings on level of

radiosensitization and GNP concentrations.

The purpose of this dissertation is to investigate whether dose inhomogeneities induced by GNPs on a cellular scale is a source of GNPs mediated radiosensitization. First, the feasibility of nanoparticle-enhanced Auger therapy was evaluated regarding electron energy spectra, microscopic dose distributions, and biological effectiveness using the S-value. Second, for nanoparticle-enhanced external photon therapy, biological effectiveness was systemically assessed in the various cell and nucleus geometry with GNPs. Radiation dose dependence of cell survival with GNPs was observed experimentally and predicted theoretically. The realistic modeling with 3D distributions of GNPs in live cells was established as observed by optical diffraction tomography (ODT).

We performed Monte Carlo simulations to characterize interactions between GNPs and low-energy photons at the nanometer scale. Calculated radiation dose was applied to a biological model to quantify the GNP radiosensitization. Due to a steep radial dose falloff within short distances from the GNPs (<1% of the surface dose at 100 nm), geometric parameters such as the shape, size, and location of the cell, nucleus, and GNPs are important to assess GNP enhanced radiation therapy. GNP – Local Effect Model was established based on live cell images and showed good agreement with observed radiation response in the presence of GNPs.

Keywords: Radiation Therapy, Nanoparticles, Monte Carlo simulation, Radiosensitizer, Biolotical Modeling

Student Number: 2013-30737

List of Tables

List of Figures

CONTENTS

Chapter III. Nanoparticle Enhanced External Photon Therapy

Chapter I. Introduction

1. Basic Principles of Radiation Therapy

Cancer is the leading cause of death around the world. Approximately 14 million new patients were diagnosed with cancer and 8.2 million patients died due to cancer in 2012. In Korea, a total of 76,855 people (27.9% of all deaths) died due to cancer in 2015. Unfortunately, cancer treatment is still one of the biggest challenges even though the science and technology of cancer treatments are continuously improving. There are three major types of treatment for cancer in modern medicine: surgery, chemotherapy, and radiation therapy.

Radiation therapy involves the use of neutral or charged particles, to deposit radiation dose. In present radiation therapy, photon and electron are most widely used particles among neutral and charged particles respectively. When photons interact with the material, they may either be transmitted without interaction or attenuated by absorption or scattering process. The number of photons interacting with a slab of material is proportional to its material thickness and a parameter known as its attenuation coefficient, which is proportional to interaction probability. There are three major photon interactions with matter in radiation therapy.

First of all, photoelectric effect is an interaction between a photon and an inner electron of the medium. The inner electron escapes from the atom with kinetic energy equal to the difference between that of the incident photon and the binding energy of the ejected electron. The mass attenuation coefficient of photoelectric effect is proportional to Z^3/E^3, where Z is the atomic number of the material and E is the incident photon energy. Photoelectric absorption is

most probable at low energies of photon and high atomic number of the material.

Secondly, while the photoelectric effect dominates photon interactions with soft tissue for low photon energies, Compton effect dominates for high photon energies. A photon interacts with loosely bound electrons. The incident photon is scattered and transfers some amounts of energy to the electron. After Compton interaction, the electron is ejected from the atom. The interaction probability of Compton effect is slowly decreasing as the incident photon energy is increasing.

Lastly, pair production occurs when the photon passes close to the nucleus of an atom. The mass attenuation coefficient is proportional to the atomic number of material and incident photon energy.

The relative importance of photoelectric, Compton and pair production for different atomic numbers of materials and photon energies are shown in Figure 1. Particularly note that these interactions can be modulated by introducing nanoparticles of different atomic numbers.

While photons interact with media via the processes described above, generated electrons deposit the radiation dose to the material. The main process by which electrons lose energy is through Coulomb interactions with either atomic electrons or atomic nuclei.

An inelastic collision occurs between incident electrons and atomic electrons. The interaction probability depends on the electron density and is generally lower for higher atomic number of materials. The rate of energy loss

in passage through water is approximately constant at 2 MeV/cm for electron energies higher than 1 MeV.

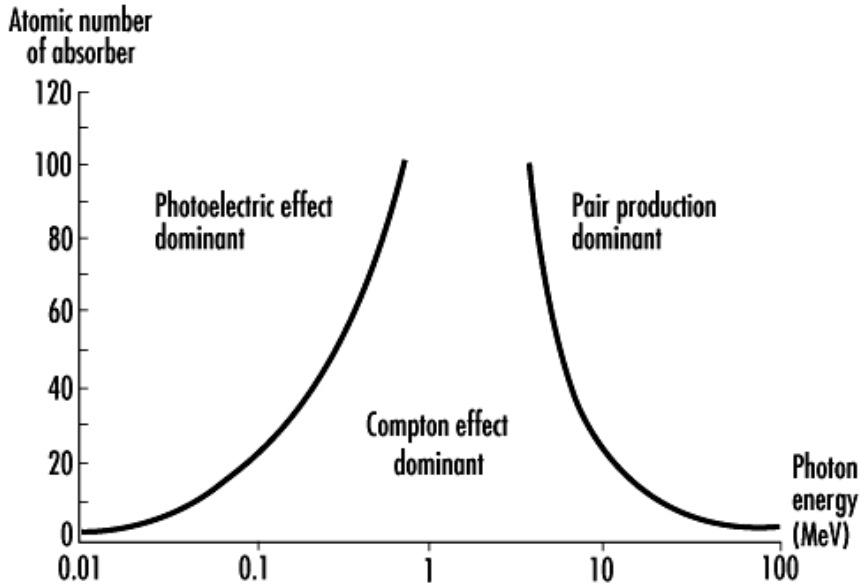

Figure 1 Relative importance of the three major photon interactions with matter (Modified from Hendee, W.R. et al., Radiation Therapy Physics, Wiley, Hoboken, JN, 2005.)

Bremsstrahlung x-ray energy loss also occurs between incident electrons and atomic nuclei. The occurrence probability of a bremsstrahlung interaction increases with electron kinetic energy and with atomic number. This is the main interaction for high energy photon beam generation. The high energy electrons collide with targets of diagnostic x-ray tubes and linear accelerator and produce bremsstrahlung high energy x-ray.

The goal of radiation therapy is to maximize radiation dose to the tumor while minimizing the dose to normal organs. To achieve this goal, various parameters are adjusted including the number of beams, beam angles, beam energies, and beam collimation. Most advanced techniques have been developed either by improving the conformity of the photon beam to the tumor such as 3D conformal radiation therapy, intensity-modulated radiation therapy (IMRT), and volumetric modulated radiation therapy (VMAT). However, by adjusting photon interactions with matter, gold nanoparticles open new possibilities to selectively increase the tumor dose.

2. Basic Principles of Radiosensitization

Ionizing radiations can cause cell death mainly by double-strand breaks. Radiation interact directly with the critical targets and cause ionization or excitation in the cell. The chain of biological damage events is initiated by radiation. This is called the direct action of radiation. Alternatively, radiation can liberate electrons from molecules in the cell to produce free radicals that are able to damage the critical targets. This is called the indirect action of radiation. The two major mechanisms of cell killing are by halting reproduction and by causing apoptosis.

A cell survival curve shows the relationship between the radiation dose and the proportion of survived cells. Among various assays used to observe the cell survival curve, clonogenic assay ("clonogenic" derived from the word "clone) is a classical method wherein the number of cells which do not lose the ability to divide even after being exposed to radiation. The cells are prepared with single – cell suspensions, which are then irradiated, often in combination with an agent. The cells are then seeded in culture dishes and allowed to grow for several weeks until visible colonies are produced. One must establish the plating efficiency which indicates the percentage of cells seeded that grew into colonies. The plating efficiency is defined as below.

$$Plating\ Efficiency = \frac{Number\ of\ colonies\ counted}{Number\ of\ cells\ seeded} \qquad \textbf{Eq. 1}$$

For example, if only 70 of 100 plated cells go on to form colonies, then the plating efficiency is considered to be 70%.

Analysis of the radiation effects requires the comparison between the number of colonies produced with irradiated cells and untreated cells. In general, the survival fraction for a particular dose is given by

$$Surviving\ fractions = \frac{Colonies\ counted}{Cells\ seeded \times Plating\ efficiency\ of\ the\ untreated\ cell} \quad \textbf{Eq. 2}$$

The graph of cell survival curve is plotted survival fraction on a logarithmic scale and dose on a linear scale as shown in figure 2. The survival curve starts out straight with finite initial slope and the curve bends at higher doses. One of proposed explanation for this "shoulder" is the linear quadratic model. The model assumes there are two targets to cell killing by radiation, one that is proportional to dose and one that is proportional to the square of the dose. According to this theory, the survival fraction can be described as below.

$$S = e^{-\alpha D - \beta D^2} \quad \textbf{Eq. 3}$$

where S is the survival fraction, D is the radiation dose, α and β are constants of the cell type of interest, which describe the initial and quadratic slope of the cell killing respectively.

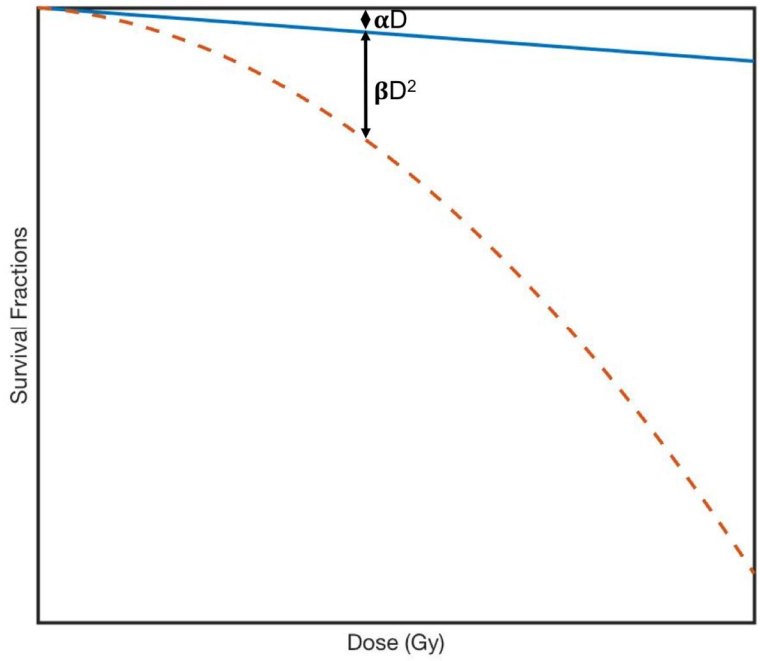

Figure 2 Cell survival curve with linear-quadratic model for nonexponential cell killing

3. Nanoparticle-Mediated Radiosensitization

For cancer treatment, the aim of radiotherapy is to maximize tumor killing while minimizing damage to healthy tissue. For the last decades, the delivery of improved physical dose distributions drove radiotherapy development. To further improve therapeutic potential of radiotherapy, interest in the use of contrast agents was stimulated by early studies which found increased damage in tissues after contrast enhanced medical imaging, indicating that the presence of a high-Z material can increase radiation damage[1]. This is attributed to the high photoelectric cross-section of these materials which means that high Z materials absorb significantly more energy per unit mass than soft tissue. Early attempts were made using thin gold foil for the use of gold as a radiosensitizers [2], but this was limited by delivery challenges to deep-seated tumors. However, nanoparticles (NPs) have been shown its potential to become trapped in tumor tissues.

The inherent toxicity of GNPs to normal tissue has been reported even though one might expect higher radiosensitization with more number of GNPs[3]. The GNPs toxicity is largely dependent on its size, surface functionalization, and administration methods. The most vulnerable organs with GNPs are the liver and spleen. This biodistribution characteristics may cause acute inflammations of the liver[4]. In vitro experimental evidence also points towards significant toxicity for GNPs. Intracellular ion release elicited by the acidic conditions of the lysosomal cellular compartment – where GNPs are abundantly internalized – is responsible for the cascading events associated with nanoparticles-induced intracellular toxicity[5]. This is called as “lysosome-enhanced Trojan horse effect” because the protective cellular

machinery designed to protect itself from foreign objects is actually responsible for their toxicity.

Due to its toxicity, the optimal concentration is a key challenge for the use of GNPs as radiotherapy sensitizer. The first experimental in vivo study supporting the use of GNPs as radiosensitizers was performed by Hainfeld and his colleagues[6]. The concentration of injected 1.9 nm GNPs was 270 mg Au/ml and the injected volume was 0.01 ml per g mouse weight. The GNPs concentrations in tumor and blood were 0.7% and 1.8% respectively by weight after injection. This study shows that the one year survival using 250 kVp x-rays with GNPs was demonstrated to be 4 times higher compared to using x-rays alone. Toxicity tests showed that mice receiving 2.7 g Au/kg lived for more than one year without overt clinical signs. This first study was followed by numerous in vivo studies seeking to characterize the effects of GNPs with ionizing radiation for therapeutic advantage without serious toxicity observance (Table 1).

Author	Hainfeld[6]	Chang	Hainfeld[7]	Hainfeld[8]	Kim
Size (nm)	1.9	13	1.9	1.9	14
GNP dose (g/kg)	2.7	0.036	2.7	4	0.3
Tumor conc. (mg/g)	7 (18 in blood)	74	7	15	0.1
Surface coating	Thiol	Citrate	Thiol	Thiol	DTPA
Cell line	EMT-6	B16F10	SCCVII	Tu-2449	CT26
Source energy	250 kVp	6 MeV e-	68 keV	100 kVp	Proton 40 MeV
Dose (Gy)	26-30	25	30	30	21
Outcome measure	1 yr OS	MS	OS	1 yr OS	1 yr OS
Group	GNP only RT only GNP+RT	Control RT only GNP+RT	RT only GNP+RT	Control RT only GNP+RT	RT only GNP+RT
Outcome	0% 20% 86%	20 days 55 days 65 days	53 days 76 days	0% 18% 56%	11-13% 58-100%

Table 1 Summary of radiosensitizing experimental in vivo data obtained with ionizing radiation and gold nanoparticles.

Several research group also conducted in vitro experimental studies combining GNPs and ionizing radiation. It was found that radiosensitized HeLa cells with 50 nm GNPs irradiated with 220 kVp x-rays gives 1.43 times greater dose enhancement than that observed for smaller GNPs[9]. Further experiments demonstrated that 1.9-nm GNPs following 225 kVp x-rays radiosensitize cells which increased the apoptotic levels[10]. Moreover, the GNPs' ability to radiosensitize tumors at clinically relevant energies (6 MV) has been shown[11]. The radiosensitizing effects of GNPs have not only been shown for cancerous cells but also for normal epithelial and endothelial cells. The functionalized Glu (thioglucose)-GNPs exposed to 200 kVp x-rays demonstrated a significant increase in non-tumorigenic cells[12]. Rahman studied the radiosensitizing effects of 1.9-nm GNPs and 80 kVp x-rays and large radiation dose enhancement (up to 24) was observed for bovine aortic endothelial cells (BAEC) with a cell proliferation assay[13].

The GNPs can be delivered to the tumor targets passively or actively. Due to the small size of the GNPs compared to the typical cutoff size of the pore (up to 400 nm) in tumor vasculature, GNPs preferentially extravasate from the vasculature at the tumor site[14]. GNPs are retained in tumor because malignant tissues have poor lymphatic drainage. This is typically known as "enhanced permeability and retention" (EPR). In vivo studies by Hainfeld et al validated the extensive retention of 1.9 nm GNPs in tumors after the blood has cleared[15]. However, smaller particles (e.g., 1.9 nm) are rapidly cleared through the kidneys and these gives the hurdle to search for alternative formation strategies, called as active targeting. The tumor-specific accumulation of GNPs can be increased through attachment of

peptides/antibodies to actively target the tumor tissues. Enhanced radiosensitization was achievable with nuclear targeting of GNPs using nuclear localization sequence peptides[16].

Chapter II. Nanoparticle Enhanced Auger Therapy

Abstract

PURPOSE: The aim of this study is to investigate the dosimetric characteristics of nanoparticle-enhanced Auger therapy.

METHODS: Monte Carlo (MC) simulations were performed to assess electron energy spectra and dose enhancement distributions around a nanoparticle. In the simulations, two types of nanoparticle structures were considered: nanoshell and nanosphere, both of which were assumed to be made of one of five elements (Fe, Ag, Gd, Au, and Pt) in various sizes (2-100 nm). Auger electron emitting radionuclides (I-125, In-111, and Tc-99m) were simulated within a nanoshell or on the surface of a nanosphere. According to MIRD (Medical Internal Radiation Dose) scheme, the cellular S-values were calculated depending on various cellular compartments with GNPs.

RESULTS: For the most promising combination of Au and I-125, the maximum dose enhancement was up to 1.3 and 3.6 for the nanoshell and the nanosphere, respectively. The dose enhancement regions were restricted within 20–100nm and 0–30nm distances from the surface of Au nanoshell and nanosphere, respectively. The dose enhancement distributions varied with the size of nanoparticles, nano-elements, and radionuclides. Cellular S-value is increased by 1.3 times when GNP is homogeneously distributed inside the cell.

CONCLUSIONS: We conclude that Auger therapy combined with nanoparticles could have the potential to provide a better therapeutic effect than conventional Auger therapy alone.

1. Introduction

As an alternative to external beam radiotherapy or brachytherapy, targeted radionuclide therapy generally utilizes α-or β-particle emitting isotopes. The isotopes conjugated with targeting agents are concentrated within the tumor while a reduced dose of radiation is given to surrounding normal tissues. However, the ranges of β-particles are larger than a typical cell diameter (~10 μm), which causes damage to healthy tissues[17]. Therefore, many researchers have been interested in Auger-electron-emitting radionuclides since Auger-electrons have ranges shorter than several hundred nanometers and a high linear energy transfer within a cell [18-21]. In addition, these Auger-electron emitters are ideal as a theragnostic agent because they can be exploited for imaging purpose either with SPECT or Positron Emission Tomography [22]. This type of targeted radionuclide therapy with Auger-electron emitters is known as Auger therapy.

Recently, another type of NP-enhanced radiation therapy was suggested, with a proposed name of NP-enhanced Auger therapy [23]. Pronschinske synthesized one-atom-thick layers of the radionuclide ^{125}I on a sheet of gold and reported large amplification of low-energy electron emission. However, a continuous atomic structure of gold sheet is physically different and may behave differently than individual NPs. Also, their simple measurement of energy distribution was not sufficient to provide quantitative insight into the

cell damage by local microscopic doses. This radial dose calculation around the NPs is a typical track-structure problem which can be solved using event-by-event Monte Carlo simulations [24, 25].

The aim of this study is to investigate microscopic dosimetric characteristics for Auger therapy combined with NPs. Using Monte Carlo simulations, we focused on the electron properties produced by Auger emitters with NPs and their microscopic dose distributions around NPs.

2. Material and Methods

2.A. Monte Carlo (MC) simulation

Simulations were carried out using GATE code version 7.1 and Geant4 version 10.1p01. The simulations were split into two steps. In the first step, either a volume or a surface source containing Auger emitters was used to irradiate nanoparticles. The NPs were in forms of either a nanoshell for the volume source (figure 3 (a)) or a nanosphere for the surface source (figure 3 (b)). The electron spectra of the three radionuclides were taken from the literature [26]. The electrons were isotropically emitted at their specific positions and a total number of simulated histories was 10^7. The electron interactions with and without NPs were scored in a phase space at the outer surface of the NP-Source geometry (i.e., the surface immediately interfaced with water). 'Geant4-Penelope' was used in the first step of the simulation [27]. This model has been proven to be an accurate low-energy model for nanodosimetry and agreed well with other event-by-event track structure codes [28-30]. For these reasons, this has been widely used to quantify nanoparticle enhanced radiation therapy [31-33]. In the second step, the previously recorded phase space was used as a source and placed at the center of a $10\times10\times10$ μm^3 water phantom (figure 3 (c)). The 'Geant4-DNA' physics was used in the step 2 simulation. This physics package tracks electrons in water of energies down to 7.4 eV and it includes a recently

updated accurate track structure model [24, 34]. G4EmDNAPhysics default constructor was used and this includes Champion elastic, Born excitation, and Born ionization model. For both Geant4-Penelope and Geant4-DNA physics, the production threshold for all particles was set to be 250 eV and atomic de-excitation including fluorescence, Auger production, and particle induced x-ray emission (PIXE) were also activated in the simulations with 250 eV threshold. The nanoscale dose was evaluated in water around the NP-Source geometry. The radial dose was scored in spherical shells having a thicknesses of 1 nm up to a distance of 1 μm from the surface of the NP-Source geometry.

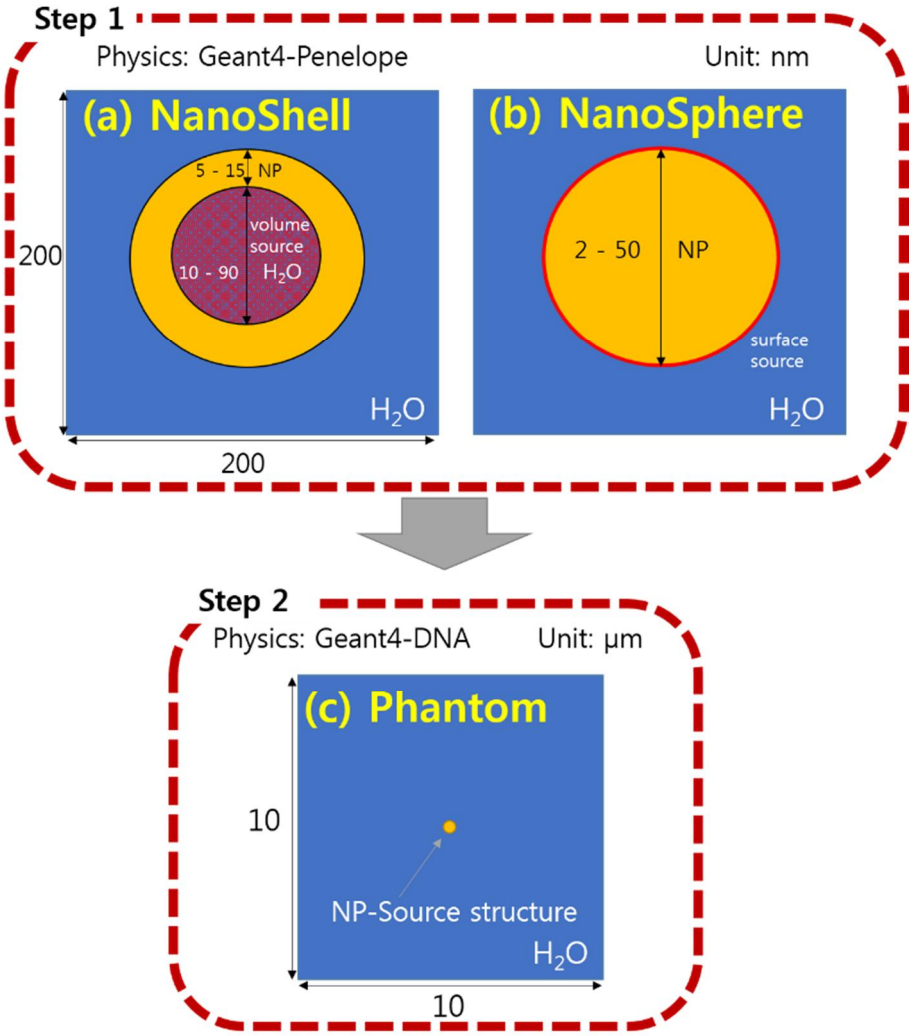

Figure 3 Illustration of simulation geometry. (a) Nanoshell encompassing water with randomly distributed isotopes. (b) Nanosphere coated with isotopes at the surface. (c) Water phantom to score deposited dose around NP-Source structure.

2.B. Simulation of Nanoparticle Structures

As mentioned before, two simulation geometries for the NP-Source structure were separately evaluated below.

2.A.a. Case 1: Nanoshell

The encapsulation of Auger emitters in a metal nanoshell was conceptually suggested for nanoparticle-enhanced Auger therapy [23, 35]. Nanoshells could be fabricated with simple galvanic replacement reactions between solutions containing metal precursor salts and Ag nanostructures prepared by polyol reactions [36]. With HAuCl4 metal precursor, gold atoms could be deposited on the surface of Ag nanosphere. During deposition, the interior Ag is oxidized and removed to produce a hollow structure. Introduction of a short aliphatic hydrocarbon chain containing I-125 and a sulfhydryl group at one end of the chain, which is known to strongly bind to gold, has been suggested [35]. The simulation (figure 3 (a)) mimicked the nanoshell geometry based on this conceptual idea [23, 35]. The volume source containing one of the three radionuclides in water was enveloped by the nanoparticle shell structure (figure 3 (a)). A nanoshell with inner/outer diameters of 10/20, 40/50, 90/100, 10/50, and 20/50 nm was separately simulated to investigate the dependence on the size of nanoshell.

2.A.b. Case 2: Nanosphere

The fabrication of a nanosphere coated with a given isotope is a well-known chemical manufacturing process. Iodine ions have a high affinity for the Au atom and thus can be effectively conjugated to GNP to form Au-I bonds on gold surfaces [37, 38]. The nanosphere coated with isotopes was shown in figure 3 (b). Four different sizes of nanosphere with a diameter of 2, 10, 20, and 50 nm were considered in our MC simulations.

2.A.c. Elements of Nanoparticle

The synthesis of iodine and Au combination is of our primary concern due to its robust chemistry reaction [39]. However, all possible combinations of five elements of nanoparticle (Au, Fe, Ag, Gd, and Pt) and three isotopes of Auger emitter (I-125, In-111, and Tc-99m) were considered. In addition, no assumptions were made about coating (e.g., PEG: Polyethylene glycol) and targeting (e.g., RGD: Arginine-glycine-aspartic acid).

The dose ratio (DR) was defined as the ratio of the doses with and without nanoparticles. In order to obtain DR, the metal nanoparticle structure of either shell or sphere was fully replaced with water, and then the whole volume of the simulation sphere was assumed to contain the isotopes, i.e., volume source. Same radioactivity level was used in the two simulations.

2.C. Cellular S-values

According to the MIRD (Medical Internal Radiation Dose) scheme,[40] the cellular S-value is defined as the dose to the target per unit cumulated activity in the source region. The spherical cell geometry was assumed: cell of 5 μm diameter and nucleus of diameter 4 μm. Various cellular compartments (nucleus, cytoplasm, surface) were considered as a source or target volumes. The S-values were calculated using the absorbed dose in the target compartment due to the energy released from the source compartment. The previously acquired radial doses from randomly distributed nanoparticles were summed to calculate absorbed dose to the target.

3. Results

Figure 4 shows the nano-scale dose distributions per emitted electron for I-125 vs. radial distances from the surface of GNP shell (40/50 nm – inner/outer diameter) and GNP sphere (50 nm diameter), and from the surface of volume source (50 nm diameter but no GNP). Due to low-energy electrons emitted from the surface of the three structures, there are very high peaks of local dose within a few nm. This indicated that the GNP sphere could enhance a microscopic dose by over 2 times in this range and by about 1.5 times at least up to 20 nm. On the other hand, the GNP shell seemed to play a role of shielding for low-energy electrons emitted from the I-125 isotopes inside it and thus showed the reduced dose distribution along the radial distances.

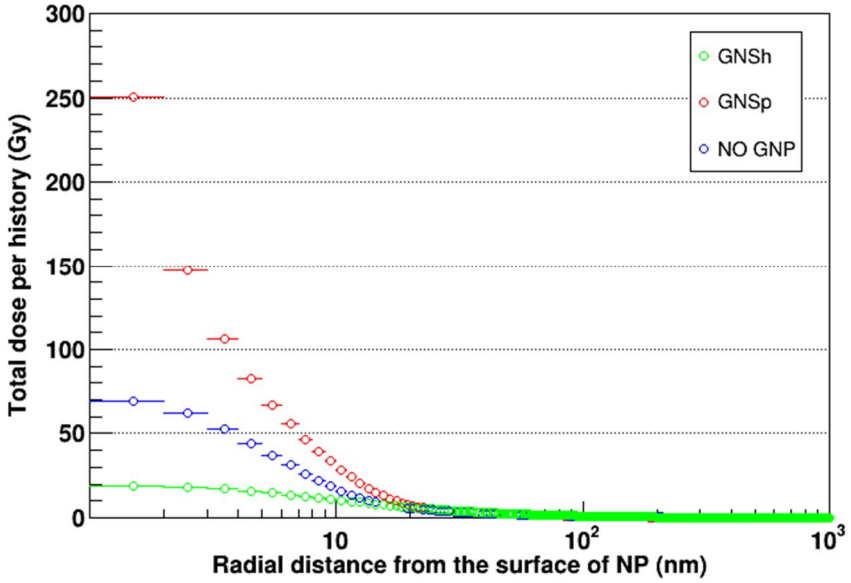

Figure 4 Total radial dose distributions with I-125 for inner 40- and outer 50-nm diameter outer diameter gold nanoparticle shell (GNSh) and 50-nm diameter gold nanoparticle sphere (GNSp) with respect to the absence of nanoparticle (labeled as NO GNP: no gold nanoparticle)

3.A. Case1: Nanoshell

Figure 5 shows two electron energy spectra obtained at the two outer interfaces; one between the Au nanoshell and water, and the other between the volume source and water. The height of the Auger peak was clearly reduced with the Au nanoshell but the number of scattered electrons was increased. As described in Table 1, when using Au nanoshells the number of electrons was decreased, while the average energy of electrons increased. This is because low energy electrons failed to leave the Au nanoshell if they have penetration range less than shell thickness.

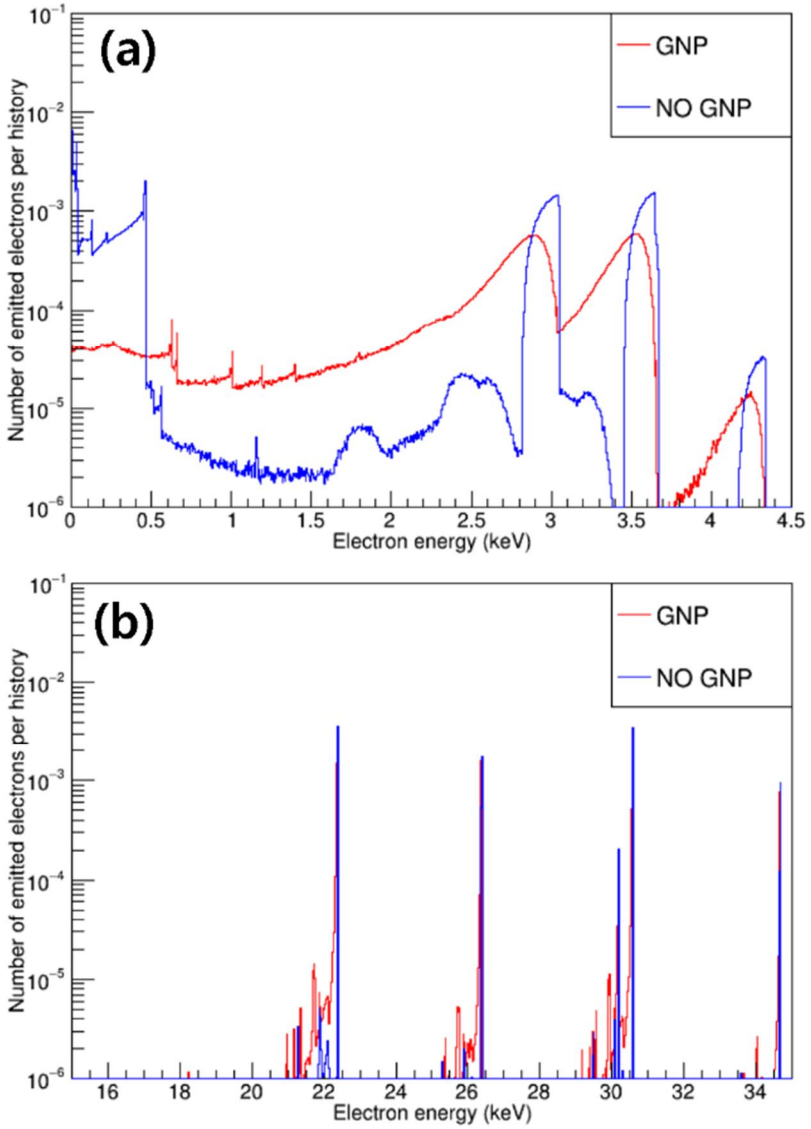

Figure 5 Electron energy spectra for I-125 obtained at two outer interfaces; one between GNP shell (inner/outer diameter: 40/50 nm) and water, and the other between volume source (diameter: 50 nm) and water in energy region of (a) 0 – 4.5 keV and (b) 15 – 35 keV. Energy region of 4.5 – 15 keV was omitted due to no electron spectra of I-125.

Nanoshells	Au		Gd		No nanoshell	
inner ϕ / outer ϕ	10/20 nm	40/50 nm	10/20 nm	40/50 nm	10/20 nm	40/50 nm
Number of electrons per history	0.11	0.11	0.14	0.12	0.29	0.19
Average electron energy (keV)	5.67	5.59	4.78	5.59	2.38	3.51

Table 2 Number of electrons per history and average electron energy for I-125 recorded at outer interfaces with nanoshells (Au, Gd) and with volume source (i.e., no nanoshell). ϕ = radius.

Figure 6 represents DR distributions along the radial distance from the surface of NP shell for various simulation setups. Overall microscopic dose shows up and down. The dose was decreased within 20 nm but rapidly increased at certain distances from nanoshell. After that, it was decreased again within larger distances from the nanoshell surface. Beyond 700-nm distances from the nanoshell surface, the presence or absence of the nanoshell did not affect the dose. The maximum amounts of dose enhancements and increased/reduced dose region were dependent on NP sizes, elements, and isotope. The effect of GNP sizes on DRs for I-125 is shown in figure 6 (a). The maximum DR values were around 1.3 for Au (20/50 nm inner/outer diameter) and dose enhancement (DR > 1) was restricted between 20 – 100 nm from the nanoparticle surface for all GNP sizes. Figure 6 (b) shows the influence of NP elements on DRs pattern for the NP shell of 40/50 – inner/outer diameter. The dependence of DR on NP elements was within +20% for 20 – 100 nm dose enhancement region and -40% for 200 – 700 nm dose reduction region. Pt and Au were found to be the best elements to maximize DR up to 1.2. For 40/50 – inner/outer diameter NP, the effects of isotopes are shown in figure 6 (c) and the maximum DR was found to be 1.2, 1.2, and 1.1 for I-125, In-111, and Tc-99m respectively. Dose enhancement regions were 20 – 100 nm, 10 - 80 nm, and 3 – 40 nm for I-125, In-111, and Tc-99m, respectively.

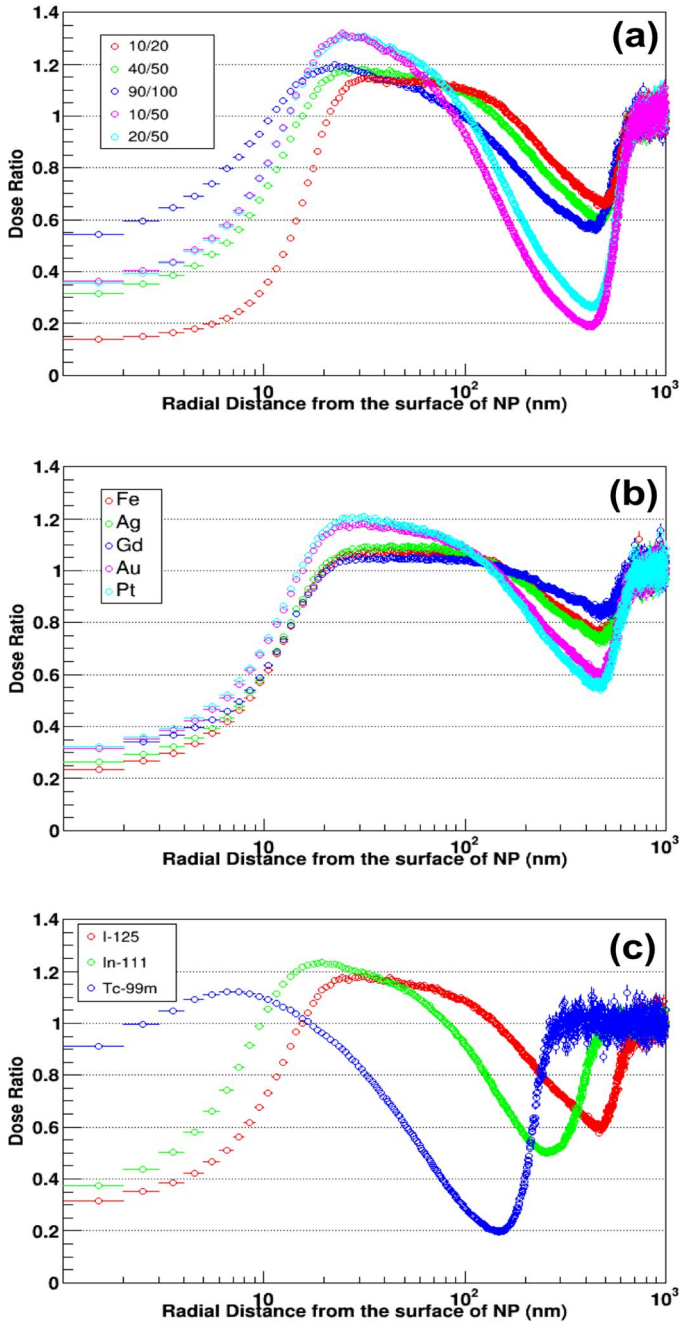

Figure 6 DRs for nanoparticle shell with respect to the absence of nanoparticle. DRs (a) for various size (labeled as inner/outer diameter) with Au - I-125, (b) for different nanoparticle elements with 40/50-nm diameters with I-125, and (c) for different isotopes with 40/50-nm diameter Au

nanoshell.

3.B. Case2: Nanosphere

The 50-nm diameter Au nanosphere generated a larger number of low-energy electrons than did the absence of nanosphere (figure 7). Since low energy electrons were absorbed less in the Au nanosphere than in the nanoshell, a larger number of low energy electrons were observed. Table 2 shows the increased number of electrons up to 3-fold and the reduced average energy with the nanosphere as compared with the absence of nanosphere. This phenomenon became more noticeable as the nanosphere size was increased. This effect is due to the higher fraction of backscatter electrons escaping from the GNP (figure 7). Also, larger amounts of electrons were absorbed inside the water compared to Auger emitters coated outside the nanoshell because electron penetration ranges in liquid water are approximately 10 and 50 nm for initial electron energy of 10 eV and 1 keV respectively [41, 42].

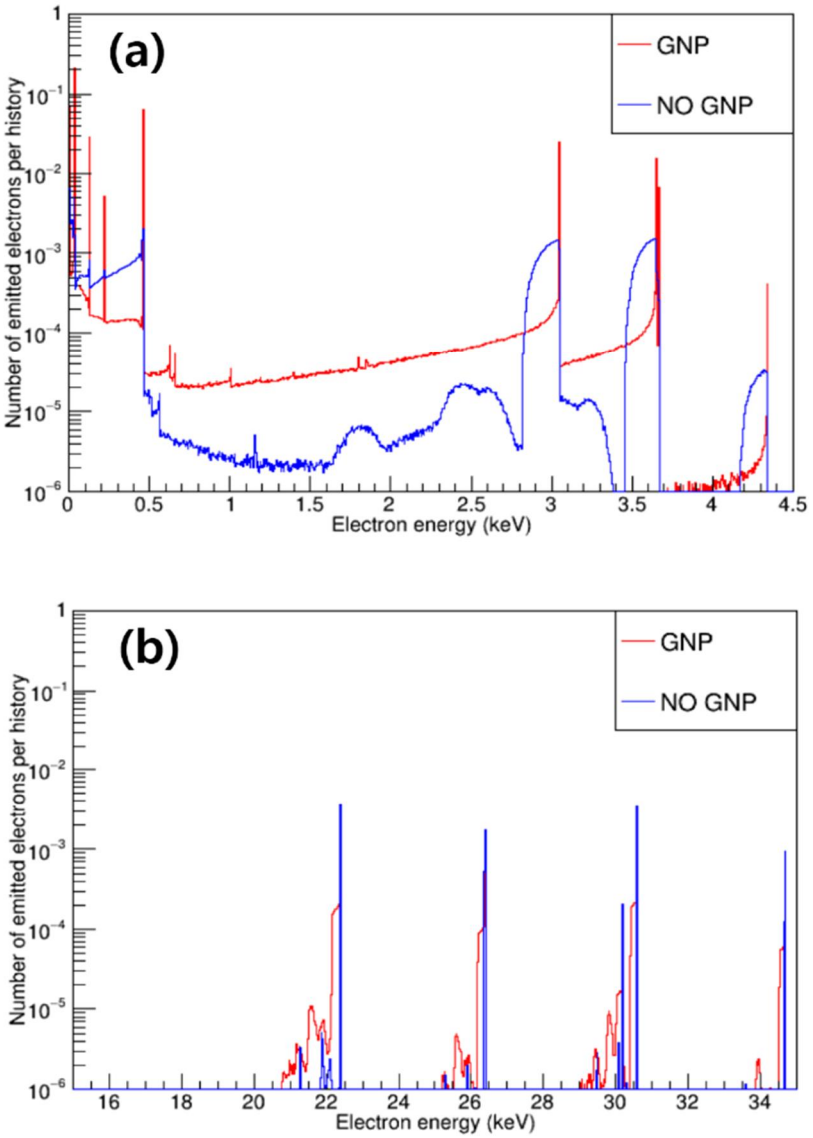

Figure 7 Electron energy spectra for I-125 obtained at two outer interfaces; one between GNP sphere (diameter: 50 nm) and water, and the other between volume source (diameter: 50 nm) and water in energy region of (a) 0 – 4.5 keV and (b) 15 – 35 keV. Energy region of 4.5 – 15 keV was omitted due to no electron spectra of I-125.

Nanosphere	Au		Gd		No nanosphere	
ϕ	2 nm	50 nm	2 nm	50 nm	2 nm	50 nm
Number of electrons per history	0.70	0.57	0.67	0.58	0.69	0.19
Average electron energy (keV)	1.05	1.15	1.11	1.20	1.07	3.51

Table 3 Number of electrons per history and average electron energy for I-125 recorded at outer interfaces with nanosphere (Au, Gd) and with volume source (i.e., no nanosphere). ϕ = radius.

Figure 8(a) shows that the DR distribution patterns varied along with changes in nanosphere size. Within 4 nm, consistent DRs higher than 1.0 were observed, but DR fluctuations were observed within 1 μm. The maximum DR was around 3.6 for 50 nm diameter nanosphere. Figure 8(b) shows that the nanoparticle material dependency was less than 10%. Figure 8(c) shows the different DR enhancement region of 50, 20, and 10 nm for I-125, In-111, and Tc-99m respectively. The isotopes DR patterns vary even within those enhancement regions.

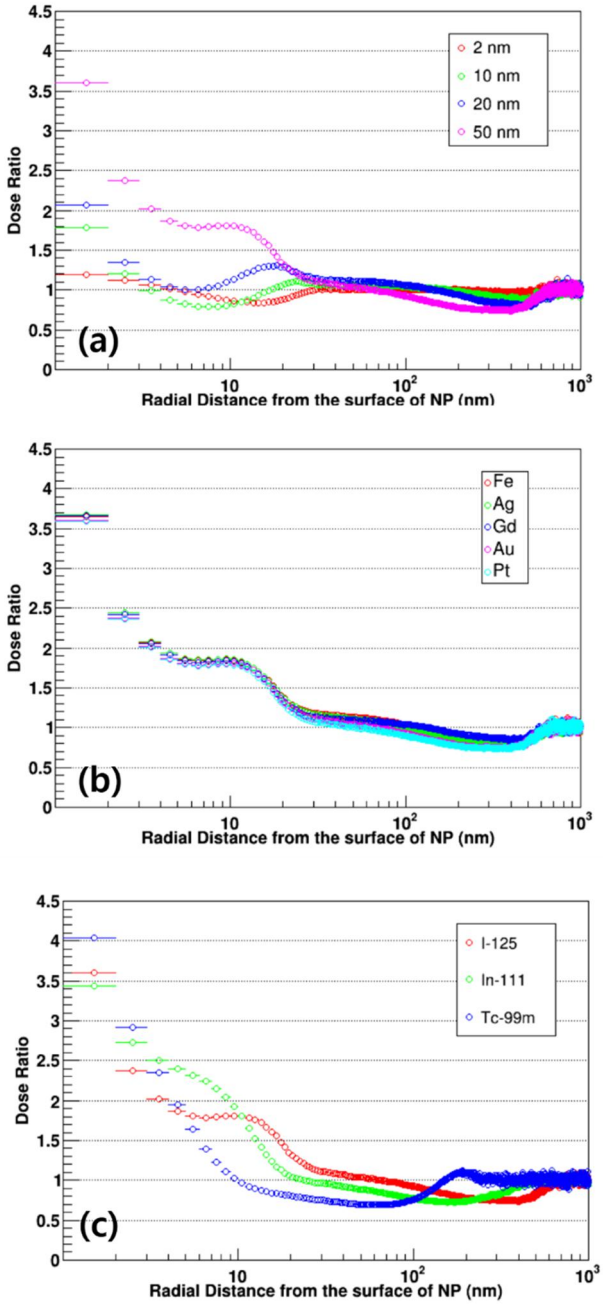

Figure 8 DRs for nanoparticle sphere with respect to the absence of nanoparticle. DRs (a) for various size (labeled as diameter) with Au - I-125, (b) for different nanoparticle elements with 50-nm diameters with I-125, and (c) for different isotopes with 50-nm diameter Au nanosphere.

2.C. Cellular S-values

Figure 9 presents cellular S-values calculations using Geant4-DNA for cells with or without GNPs. The highest difference between them was observed 30% for cell source to cell target. Their cellular S-values are 3.50×10^{-3} Gy/Bq/s and 4.56×10^{-3} Gy/Bq/s for S(C<-C) without and with GNPs respectively. The maximum S-value achieved was to 8.46×10^{-3} Gy/Bq/s for S(N<-N) with GNPs conditions.

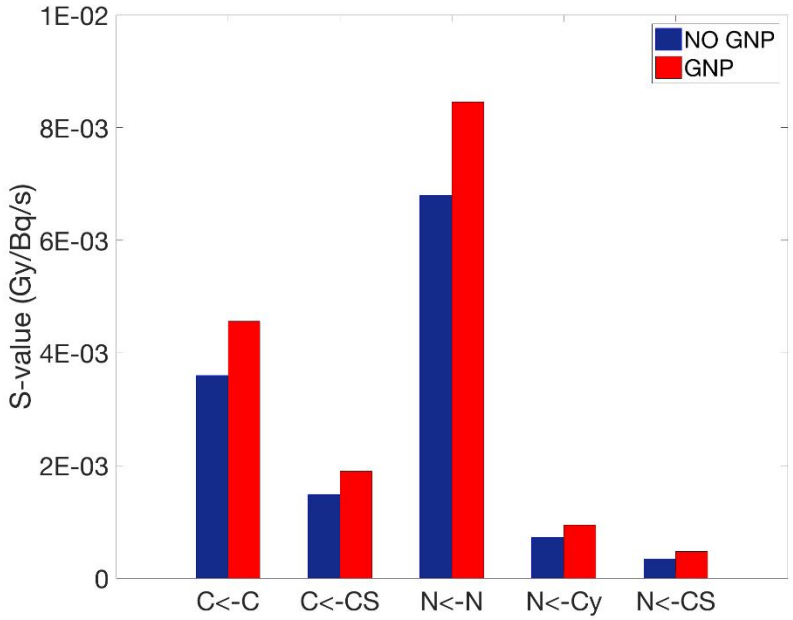

Figure 9 Cellular S-value for various target <- source combinations (C: cell, CS: cell surface, N: nucleus, Cy: cytoplasm) between without/with gold nanoparticles (NO GNP/GNP)

4. Discussion

Targeted radionuclide therapy, especially Auger therapy, allows minimal residual damage by taking advantage of the nano-scale range of Auger-electrons in tissues. Therefore, the success of Auger therapy depends on not only the microscopic distribution of Auger emitters within a target cell but also the electron energy spectrum (i.e., electron ranges). The manipulation of energy spectra has been limited only to the selection of radionuclides. However, owing to the recent advancement in nano-medicine, nanoparticles themselves could be an effective targeting agency of radionuclides. In addition, as shown in this study they might be used to change the electron energy spectrum, which may open new applications in Auger therapy [23]. In this study, dissociative electron attachment process was also not evaluated for chemical processes. The free radical damage to DNA strand breaks is one of the main concerns for low-energy electron therapy [43]. However, it is obviously important to bring nanoparticles in close proximity to the cells because dose enhancement was generally observed within 100 nm from the nanoparticles. Note that the dose deposition pattern around nanoparticles shown in this study may not directly correlate to the cell survival if a proper biological model based on a nano-scale distribution of NPs is not suggested.

For effective NP-enhanced Auger therapy, it was shown that nanosphere is generally superior to nanoshell in terms of maximum DRs (e.g., about a maximum dose factor 3 between 50 nm Au nanosphere and 50/10 nm Au nanosphere) in close proximity to the nanoparticle surface. For nanosphere, however, the impact of the deiodination should be investigated because it

reduces the concentrations of iodine, leading to low radioactivity [44]. On the other hand, methods have to be further developed to keep the iodine bound only inside the nanoshell or outside the nanosphere [35]. Regarding element – isotope combinations, Au – I is not only recommended in terms of larger dose enhancements region in this study but also due to their strong chemical bonds [38].

This study employed the average Auger emission spectra from the Howell's AAPM report which included the O-shell contribution to best meet our MC simulations [26]. Different theoretical methods for Auger emission spectra may yield slightly different dose distributions. More accurate Auger emission spectra are necessary for Monte Carlo simulations. Also, since 'Geant4-Penelope' code neglect condensed-phase effects, this results only provide a crude approximation to low-energy electron transports in NPs. Further studies will be necessary to quantify the influence of NPs reduced dimensionality on interactions of low-energy electrons [45, 46]. The minimum production threshold of Geant4-Penelope was set to 250 eV, which corresponds to a range in water of a few nm. This is the low energy limit of GATE v7.1. As a result, this can lead to an underestimation of the dose within a few nm from the nanoparticle surface.

A new version of Geant4-DNA physics model recently became available [47, 48]. If it had been used in this study, dose calculation around the NPs in step 2 would have been impacted but effects are expected to be diminished to calculate relative dose ratio. Models and simulation code have been developed for metallic systems but they are not publicly accessible [49, 50]. Therefore, the development of open-source Geant4-DNA physics for metals is highly

necessary and will improve the results of dose calculation especially in close proximity to a metal NP in the future.

Target candidates for NP-enhanced Auger therapy can be chromosomes in extended form (~ 300 nm) and mitochondria (~ 300 nm) in tumor cells. The critical target in Auger therapy has been the nuclear DNA of tumor cells [19, 51]. Due to the short range of Auger-electrons, methods for allowing NP internalization into the cell nucleus are crucial [52]. Recently, GNP targeting with pH Low-Insertion Peptide (pHLIP) showed promising results of internalization into cell membrane [53] and the triple targeting method (cell, nucleus, and DNA) was also developed to improve targeting biomolecules to the DNA [54]. Additionally, mitochondria have been shown to exhibit altered function and even induce apoptosis when exposed to ionizing radiation [55, 56]. The recent work of Wang et al shows evidence of Au nano-rods being selectively taken up in the mitochondria of lung carcinoma cells (A549) [57] and Kirkby et al investigated mitochondria damage by GNP with external radiotherapy [58]. Therefore, mitochondria may be a possible non-DNA target to cause cell killing.

5. Conclusions

The NPs combined with Auger emitters can greatly alter the energy spectrum of electrons near the NPs and thus the microscopic dose distributions around the surface of NPs. From dose enhancement point of view, maximum dose enhancement up to 1.4 was achievable with Pt (10/50 nm inner/outer diameter) nanoshell and In-111. On the other hand, for nanosphere, any material NPs (50 nm diameter) and Tc-99m lead dose enhancement up to 4.0. For Au and I-125 combination, the average microscopic dose enhancement using the Au nanoshell (40/50 nm inner/outer diameter) and the nanosphere (50 nm diameter) was 1.1 and 1.3, respectively, within the enhanced region from the surface of NP with I-125. For the combination of Au and I-125, the maximum dose enhancement was up to 1.3 and 3.6 for nanoshell and nanosphere, respectively.

In the region of > 100 nm from the surface of GNP, the local microscopic doses were shown to decrease, which should be carefully taken into account for biological modeling. The effect would only be enhanced when Au – ^{125}I nanoparticles are adequately internalized in the cells. Therefore, we conclude that Auger therapy combined with nanoparticles could have a potential to provide a better therapeutic effect than the conventional Auger therapy.

Chapter III. Nanoparticles Enhanced External Photon Therapy

Abstract

PURPOSE: To systematically assess the biological effectiveness of GNPs distributed in the extracellular media for realistic cell geometries

METHODS: TOPAS-nBio simulations were used to determine the nanometre-scale radial dose distributions around the GNPs, which were subsequently used to predict the radiation dose response of cells surrounded by GNPs. MDA-MB-231 human breast cancer cells and F-98 rat glioma cells were used as models to assess different cell geometries by changing 1) the cell shape, 2) the nucleus location within the cell, 3) the size of GNPs, and 4) the photon energy.

RESULTS: The results showed that the sensitivity enhancement ratio (SER) was increased up to a factor of 1.2 when the location of the nucleus is close to the cell membrane for elliptical-shaped cells. Heat-maps of damage-likelihoods showed that most of the lethal events occur in the regions of the nuclei closest to the membrane, potentially causing highly clustered damage patterns. The effect of the GNP size on radiosensitization was limited when the GNPs were located outside the cell. The improved modeling of the cell geometry was shown to be crucial because the dose enhancement caused by GNPs falls off rapidly with distance from the GNPs.

CONCLUSIONS: We conclude that radiosensitization can be achieved for kV photons even without cellular uptake of GNPs when the nucleus is shifted towards the cell membrane. Furthermore, the damage was found to concentrate in a small region of the nucleus in close proximity to the

extracellular, GNP-laden region.

1. Introduction

2.A. Nanoparticle Mediated Radiosensitization

The goal of radiation therapy is to deliver therapeutic doses to tumors while sparing surrounding normal tissue. In current medical practice, various techniques such as intensity-modulated radiation therapy (IMRT) are applied to achieve highly conformal dose distributions. To further the therapeutic ratio further, nanoparticles (NPs) have been suggested to increase the dose to the target. Two methods can be used to achieve a NP concentration gradient between tumors and healthy tissue. First, NPs may accumulate passively in tumors due to the enhanced permeability and retention (EPR) effect [59]. Second, the NPs can be coated with targeting molecules that attach to features only expressed by tumor cells. One of the most common materials considered for NPs radiosensitization is gold. Gold nanoparticles (GNPs) are of interest due to their low toxicity, easy surface modifications and, a large photoelectric cross sections [60, 61]. Numerous in vitro [9, 11, 62], in vivo [6, 8, 61], and in silico [32, 63, 64] studies have shown amplification of biological damage in irradiated cells in the presence of GNPs.

In in silico studies, Monte Carlo simulations and analytic calculations were used to calculate dose distributions around NPs. Even though the highest dose enhancement was observed in the immediate proximity of a GNP, an increase in dose up to 10 μm from the surface of the irradiated GNP was observed due to the production and emission of secondary electrons from the GNPs [65, 66]. The amount of dose enhancement induced by GNPs has been investigated for

multiple modalities, including kV and MV photon and proton irradiations as well as Auger therapy [33, 67, 68]. Due to the high cross section of the photoelectric effect in gold, photons of kVp energy have been proven to be more effective for GNP enhanced radiation therapy [11, 66]. For this reason, effective GNP-enhanced radiation therapy using low-energy photons is more clinically feasible for shallow-seated tumors such as breast cancer and glioma near the skull. In particular, for glioma and glioblastoma treatments GNPs can be injected directly at the site of surgery, which greatly reduces complications in penetrating the blood-brain barrier to deliver the GNPs to the target [69]. GNPs injected at the excision site diffuse into the interstitial fluid, following the spread of the tumor cells.

In order to model cell radiosensitization with GNPs, an approach based on the Local Effect Model (LEM) was applied to consider the effects of highly inhomogeneous dose distributions at the sub-cellular scale generated by the presence of GNPs, the GNP-LEM [32, 63, 64], and to investigate other potential radiation targets such as mitochondria and blood vessels. These previous studies all assumed a spherical shaped cell with a centrally located nucleus and predicted the decrease in cell survival in the presence of GNPs. However, the spherical cell geometry used in those studies was overly simplified. The nucleus, which contains radiation sensitive targets such as DNA, is often located at the periphery of a cell. In addition, tumor cells are not typically spherical in shape but can have complex shapes. To the best of our knowledge, there have been no systematic studies to quantify the dependency of GNP radiosensitization on the cell geometry.

In this study, we follow the GNP-LEM approach to quantify biological effects depending on 1) the shape of the cell membrane, 2) the location of the nucleus, 3) the size of GNPs in the media, and 4) the photon source energy. Additionally, we studied the heat-map of damage induction within the nucleus.

2.B. Local Effect Model

A major reason for the application of heavy ion beams is their increased relative biological effectiveness (RBE) in the Bragg peak region. Hence, a biophysical model is necessary to calculate biologically effective dose to the tumor and improve clinical outcomes of treated patients. One of the successful models was so-called 'Local Effect Model' (LEM) implemented in the treatment planning at the Gesellschaft für Schwerionenforschung (GSI, Darmstadt, Germany).

The goal of LEM is to derive the biological effects of ion radiation from the response of cells or tissues to photon radiation (Figure 10). The main assumption of the LEM is that equal local doses should lead to same local effects, independent of the radiation quality. The local dose is calculated as a dose function of the radial distance to the particle track. The total microscopic local dose distributions in the cell are calculated by superimposition of the track position and its radial dose function. Assuming that the cell nucleus is the sensitive target of the observed radiation effects, one can calculate the biological effectiveness of particles with the average local effects within the nucleus.

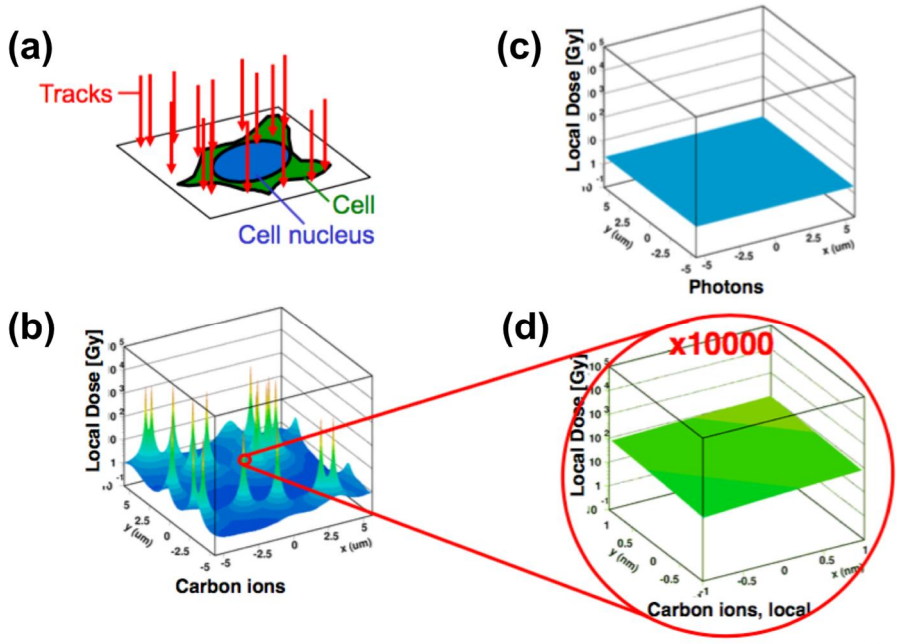

Figure 10 Schematics of Local Effect Model (a) Random distributions of particle tracks transverse through the cell (b) Corresponding track produce extremely high local dose spikes (c) The local dose distributions of photon is expected to be flat (d) The local distributions of particles can also be approximated by a flat one. (Modified from M. Scholz, Radiation Quality in Ion Beam Therapy, EURADOS Winter School 2014)

2.C. Optical Diffraction Tomography

Three-dimensional (3D) optical microscopy techniques have been an invaluable tool in modern biomedicine sciences. Among various novel techniques, optical diffraction tomography (ODT) has demonstrated 3D live cell imaging. ODT has rapidly gained significant interests due to the following reasons:

- ODT does not require the use of exogenous labeling agents such as fluorescence protein and quantum dots. Thus the characteristics of the cell are not altered.
- ODT provides quantitative imaging properties of the cells. Refractive index (RI), intrinsic optical properties of the material, is used as an imaging contrast in ODT.

ODT was first theoretically proposed in 1969 by E. Wolf and experimentally demonstrated from the late 1970s. With recent technical advances in laser sources, detecting devices, and computer powers, the field of ODT has been expanded to biophysics and cell biology.

The principle of ODT is similar to X-ray computed tomography (CT) because they use the same governing equation, Helmholtz equation (Figure 11). ODT utilizes visible light to measure light scattering by the object. The 3D RI distribution image of the sample is inversely reconstructed from the multiple 2D optical holograms obtained with various illumination angles.

	X-ray Computed Tomography	Optical Diffraction Tomography
Schematics	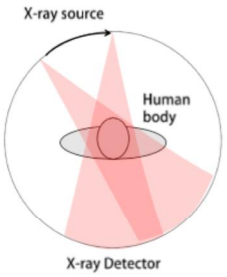	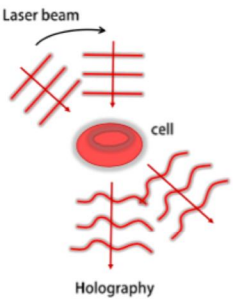
Governing Equation	Helmholtz Equation	
Source	Incoherent X-ray	Coherent Laser
Detector	X-ray image sensor	Optical image sensor
Raw images	2D Intensity images	2D Optical Holograms
Imaging contrast	Absorptivity	Refractive Index

Figure 11 Comparison between X-ray CT and ODT (Modified from Ref [78])

2. Material and Methods

2.A. Theoretical Modeling

2.A.a Monte Carlo Simulation

Monte Carlo simulations were performed using the alpha version of TOPAS-nBio, an extension of TOPAS (Tool for Particle Simulation). We used TOPAS version 3.0.1, which is layered on top of Geant4 version 10.2.p1.[70] TOPAS-nBio is a nanometre scale extension[71] to TOPAS for nanometre scale simulations using the Geant4-DNA[24, 34] physics processes. The simulation procedures were the same as in our previous work[32, 33] and are briefly described (Figure 11).

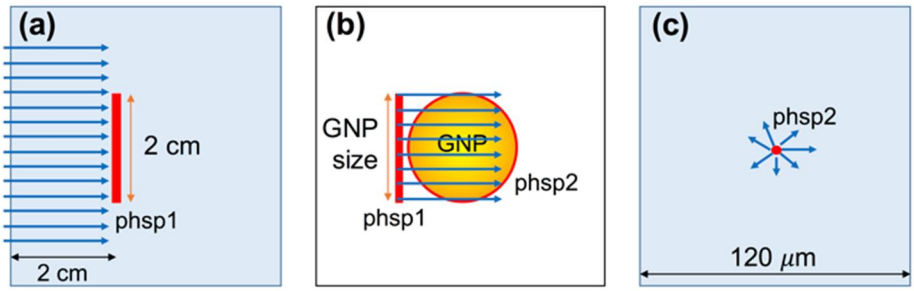

Figure 12 Schematic diagram of simulation geometry (not in scale) (a) For 150 kVp and 51 keV photon beams, the phase space were recorded for particles passing a 2 cm diameter area at 2 cm depth in a macroscopic water phantom. (b) The radiation field was reduced to the size of GNP and irradiated into GNP in vacuum. The outgoing electrons were scored in a second phase space file on the surface of GNP. (c) The second phase space was used as source in a microscopic water phantom.

Three-photon sources were investigated: (1) a 150 kVp polychromatic beam with a 2 mm aluminum filter acquired by SpekCalc 1.125, (2) a 51 keV mono-energetic beam, and (3) a Varian TrueBeam (Varian Medical Systems, Inc., Palo Alto, CA) 6 MV beam downloaded from the manufacturer website (at myvarian.com/montecarlo)[72]. The first two beam energies were selected to match the experimental setup that determined the cell-response parameters of MDA-MB-231 and F-98 cells, respectively. A cylindrical water phantom was simulated with impinging uniform photon beams of 50 mm in diameter. All particles passing through a circle of 10 mm radius centered on and perpendicular to the beam axis within the phantom was recorded. The phase space files were acquired at 2 cm depth to reflect clinical treatment conditions for shallow tumor such as breast cancer (Figure 11(a))[73, 74]. For kV photons, the percent depth doses and energy spectra at 2, 5, and 10 cm depth are shown in Figure 12. The normalized energy spectra at different depths do not differ significantly, particularly in the region of highest interaction probability (~40-100 keV). Therefore, the relative results in this study are expected to be valid for other depths.

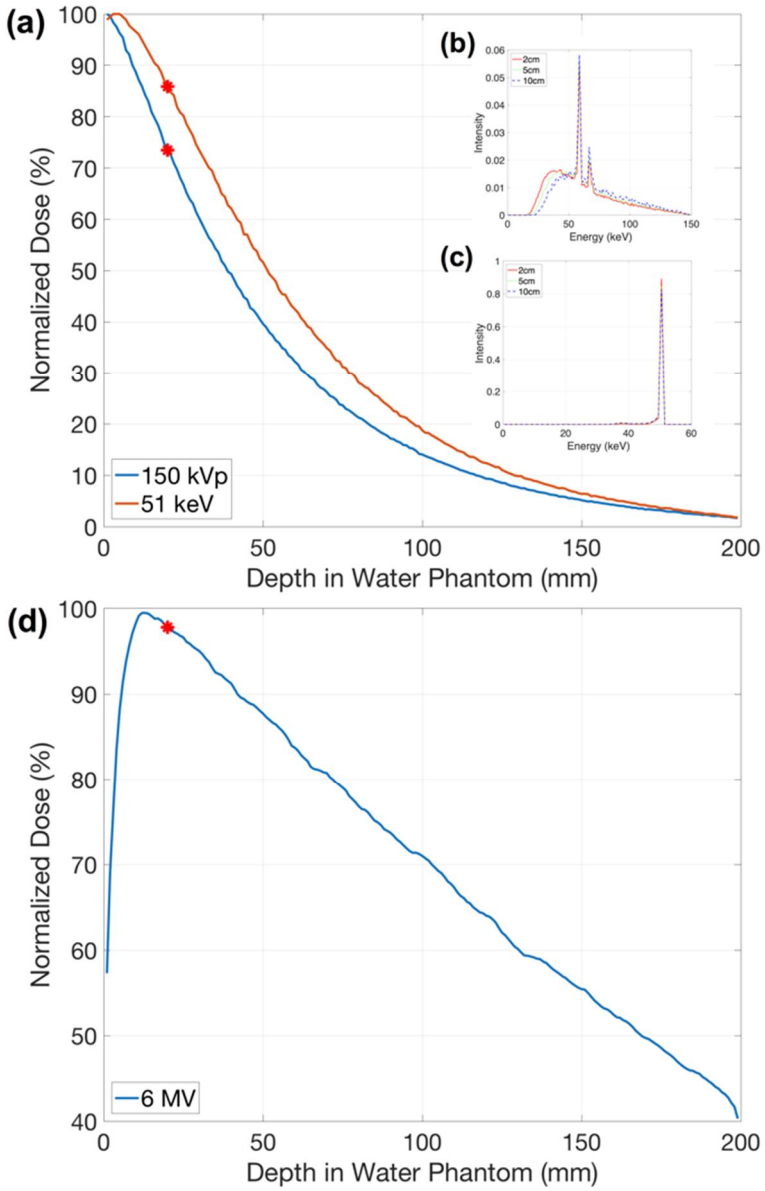

Figure 13 Percentage depth dose for (a) 150 kVp and 51 keV photon beams. Normalized energy spectra of (b) 150 kVp and (c) 51 keV at 2, 5, and 10 cm depths. Percentage depth dose for (d) 6 MV photon beam. The phase space files were recorded at 2 cm depth as indicated by red dots.

The radius of the phase space acquired in the previous step was adjusted to have the same diameter as a single GNP (diameter = 2, 15, 20, 50 nm) and was used to irradiate a single GNP (Figure 11(b)). The momentum directions of the particles were forced to be parallel to the forward beam direction to ensure that all particles pass through the GNP. Following our previous work,[33] each particle was weighted by 1/cos(θ) based on the angle (θ) between its original direction and the beam axis to account for contributions of laterally scattered electrons. Electrons exiting the GNP were recorded in a second phase space file covering the outer surface of the whole GNP. The phase space recorded on the GNP surface was used as a source at the centre of a 120 × 120 × 120 μm3 water phantom (Figure 11(c)).

The radial dose up to 50 μm from the surface of GNP was calculated in spherical shells with a thickness of 1 nm up to 50 μm from the surface of the GNP. Based on the obtained radial dose distributions, analytic functions were derived to describe the radial dose originating from the GNPs for effect modeling to reduce computation time. The form of the analytic functions was $Dose = a \cdot (radius)^b + c$ where a, b, and c are constants for different sections of radial ranges.

For the simulations in gold, the Geant4 low-energy electromagnetic Penelope physics model was used and electrons were tracked down to 100 eV.[28-30] The range cut for the production of all particles was set to 1 nm. The standard TOPAS-nBio Geant4-DNA physics list was used to track electrons in water.[24, 34]

In all the above simulations, atomic de-excitation processes were activated including fluorescence, Auger electron emission, and Auger cascades.

2.A.b Effect Modeling

The interaction probability per dose was calculated as below.

$$P_{interaction} = \left(\frac{R_{GNP}}{R_{phsp}}\right)^2 \times N_{track} \qquad \textbf{Eq. 4}$$

The total interaction probability was determined by two factors: the probability that a random photon in our phase space passes through a GNP and that a photon passing the GNP interacts. The first factor accounted for the difference in size of the scored phase space in the macroscopic scale water phantom to the microscopic size of the source phase space for GNP irradiation. Here R_{GNP} was the radius of the GNP and R_{phsp} was the radius of the phase space acquired in a macroscopic water phantom. For example, for 15 nm diameter GNP, R_{GNP} and R_{phsp} were 7.5 nm and 10 mm respectively. The second factor is determined by the particles interacting in the microscopic volume of the GNP. Here N_{track} was defined as the number of particle tracks that interacted and caused an ionization in the GNP volume for incoming particles depositing 1 Gy in a water phantom.

The LEM was developed to predict the relative biological effectiveness in particle therapy and has subsequently been applied to calculate effect enhancements due to GNPs [32, 64]. The basic assumption of the LEM is that equal local doses on a sub-cellular scale lead to equal local damages, independent of the energy and type of radiation. The LEM describes the damage in terms of "lethal events (N)" which is a function of dose (D) and follows a Poisson distribution. The macroscopic surviving fraction with GNP can be described by

$$S_{GNP}(D) = e^{-\overline{N(D)}} \quad \textbf{Eq. 5}$$

where $\overline{N}$ is the average number of lethal events in the sensitive target.

In the LEM (and thus GNP-LEM), the average number of lethal events in the sensitive target is assumed to be the integral of the number of events locally determined by an empirical dose-response curve for x-ray, which is given below:

$$\overline{N(D)} = \int_V \frac{N(D)}{V} dV = \int_V \frac{-\ln(S_x(D))}{V} dV \quad \textbf{Eq. 6}$$

Since linear-quadratic (LQ) model overestimates the response in the high-dose region, the dose-response curve is represented in two ways with a threshold dose D_t and maximum slope $S_{max}=\alpha+2\beta D_t$ as follows:

$$S_x(D) = \begin{cases} e^{-\alpha D-\beta D^2} & (D \le D_t) \\ e^{-\alpha D_t-\beta D_t^2} e^{S_{max}(D-D_t)} & (D > D_t) \end{cases} \quad \textbf{Eq. 7}$$

For GNP enhanced radiation therapy, the local dose distribution can be described by a summation of the homogeneously delivered prescription dose and the additional dose from interactions with the GNPs. This additional dose was determined by the summation of the radial dose per single ionizing event for each GNP multiplied by the interaction probability per delivered dose and the prescribed dose. Here the radial dose was calculated with Monte Carlo simulations described in the previous section. The conceptual diagram of GNP-LEM is described in Figure 14.

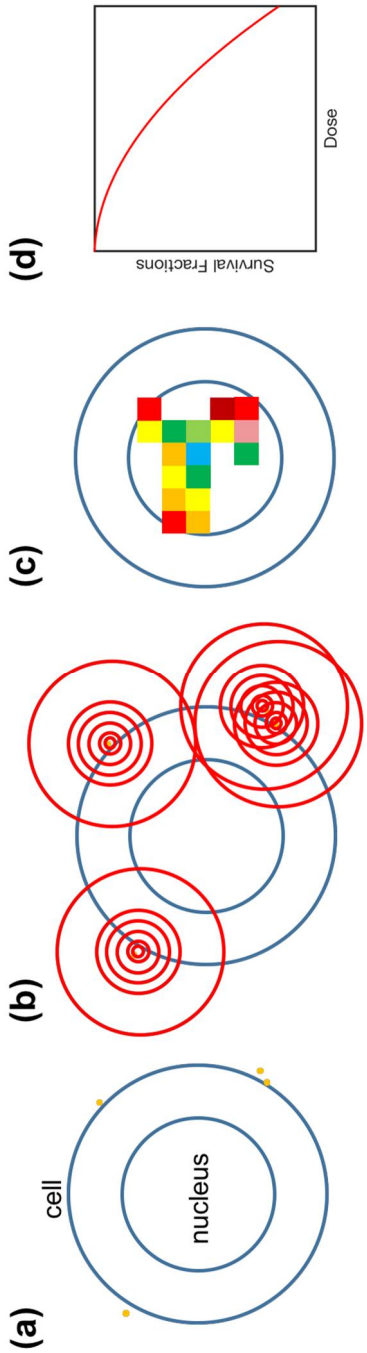

Figure 14 Conceptual diagram of Gold Nanoparticle – Local Effect Model

The two-dimensional GNP-LEM was developed using area integration. This is a reasonable assumption for in vitro experimentation with cells in 2D Petri dishes.

2.A.c Input Parameters

Two cell lines were chosen to study the geometrical effects, MDA-MB-231 breast cancer and F-98 glioma cells. These cells were used because their radiation response in the presence of GNPs has been previously investigated.[11, 69] The parameters for the LQ model were α = 0.019, β= 0.052 and α = 0.002, β= 0.079 for MDA-MB-231 irradiated with 150 kVp and 6 MV photons, respectively.[11] They were α = 0.002 and β= 0.041 for F-98 irradiated with 51 keV.[75] As no α and β values for 6 MV are published for F-98 cell lines, we assumed same α and β values as 51 keV exposures. The threshold dose D_t, which typically is in the range of 10 to 30 Gy, was set to 20 Gy for this study.[76]

We used the cell diameters of 13.5 and 32.5 µm with nuclei of 8 and 10 µm in diameter for MDA-MB-231 and F-98 cells, respectively.[77] Based on microscopic images we know that these cells often have an elliptical shape, which was considered in our modeling approach. For elliptical cell geometries, the cell membrane diameter was constantly changed for major and minor diameter. The extracellular media was represented by a thickness of 2.5 µm around the cell membrane. The cell geometry was assumed to be a cylinder with a thickness of 2 µm and considered as a two-dimensional flattened object for GNP-LEM. Table 3 summarized the geometry setup.

		Cell diameter [µm]	Nucleus diameter [µm]
Circle	MDA-MB-231	13.5	8
	F-98	32.5	10.5
Ellipse	MDA-MB-231	15.5/11.5, 17/10, 18.5/8.5	8
	F-98	37/28, 40.5/24.5, 44/20.5	10.5

Table 4 Summary of the geometrical setup. For the ellipse, the major and minor diameters are given.

Various cell geometry conditions were considered for the effect modeling (Figure 15). First, the effects of cell membrane shapes were investigated in terms of eccentricity $e = \sqrt{1 - b^2/a^2}$ where a and b are the major and minor axis half lengths (Figure 15(a) and (d)). Secondly, the nucleus was shifted inside the cell (Figure 15(b), (e), and (f)). The radiosensitization effects of several distances (d) between the center of the cell and the nucleus were investigated. Two directional locations were considered along the major and minor axis due to asymmetric features of elliptical cells (Figure 15(e) and (f)). Due to geometrical symmetries, results for shifts of the nucleus along other directions are expected to be bracketed by these two scenarios. To determine the regions of importance for the GNP enhancement effect inside the nucleus we calculated not only mean dose enhancement in sub-regions (Figure 15(c), (e), and (f)) but also the heat map of lethal events across the nucleus.

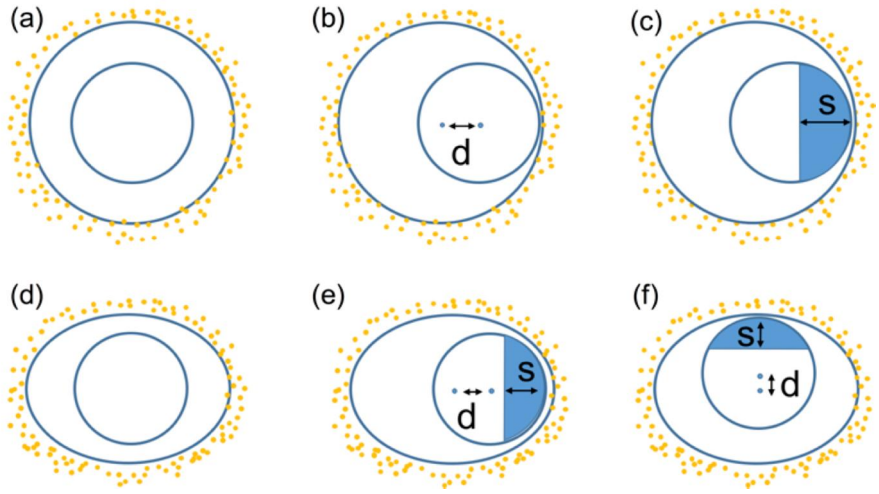

Figure 15 Schematic diagram of cell and nucleus used for the GNP-LEM. (a): Circular cell with centrally located nucleus; (b): Circular cell with shifted nucleus; (c): Circular cell with shifted nucleus and sub-regions in the nucleus; (d)-(f): Similar for elliptical cell with nucleus shifted along major and minor axis (d = distance between center of cell and nucleus). The parameter s gives the size of the sub-regions in the nucleus to calculate mean dose enhancement.

For all scenarios, NPs were randomly distributed outside the cell membrane in the cylindrical extracellular media and 2% mass weight concentrations of GNPs to the total cell and media were assumed. The number of GNPs was calculated from the 2% mass weight, volume and density of GNPs, and those of the cell and extracellular media. We considered a GNP size of 15 nm in diameter as a reference because this size was used in several in vivo studies. [8, 78] The GNP diameters of 2, 20 and 50 nm were also considered to investigate the impact of the GNP size. The geometrical components including cell, nucleus, and randomly placed GNPs were modeled in MATLAB 2016b (Mathworks, Inc., Natick, MA).

Dose-response curves were calculated for various scenarios with GNP-LEM predictions. The sensitivity enhancement ratio (SER) was defined as the different ratios of the area under the dose-response curve. To evaluate the importance of the sub-regions, the mean dose enhancement factor (MDEF) was defined. The MDEF was calculated by dividing the dose in a sub-region in the presence of GNPs by dose without GNPs. The lethal event heat-map with/without GNPs was also calculated to show the inhomogeneous distribution of GNP-induced lethal events inside the nucleus.

2.B. Biological Experiments

2.B.a Cell and Gold Nanoparticles

MDA-MB-231 breast cancer cells were cultured in Rosewell Park Memorial Institute medium 1640 (RPMI-1640) supplemented with 10% fetal bovine serum and 1% penicillin/streptomycin. Cells were maintained in a tissue culture incubator at 37°C with 5% CO_2/95% air.

Spherical Aurovist^{TM} 1.9-nm GNPs used in previous studies were purchased from Nanoprobes Inc. (Yaphank, NY, United States). According to manufacturer's instructions, GNPs were suspended in sterile water, filtered through a provided filter and stored at -20 °C.

2.B.b Inductively Coupled Plasma – Mass Spectrometry

A total of 2.2×10^{-6} cells were plated for 24 h then exposed to 500 μg/ml concentrations of GNPs for 24h, washed two times in phosphate buffered saline (PBS), trypsinized, counted, and digested in *aqua regia*. Gold content was determined using a Perkin Elmer SCIEX Inductively Coupled Plasma Mass Spectrometry (Shelton, CT, United States).

2.B.c Clonogenic Survival Assays

Radiosensitization was evaluated by clonogenic survival at kV photon energies. Cells were incubated for 24 h and treated with 500 μg/ml of 1.9 nm GNPs and incubated for 24 h prior to irradiation. These cells were irradiated with 150 kVp photons with 2 mm filter by using X-RAD 320 (Precision X-ray, North Branford, CT, United States). After irradiations, the cells were

incubated for 14 days and the change of medium during incubation was carried out after 7 days. The resulting cell colonies were stained with crystal violet (0.5% w/v) and counted. Survival fractions were then calculated relative to unirradiated cells.

2.B.d Western blot analysis

Cells were plated in 100 pi dishes in culture medium (RPMI) supplemented with 10% fetal bovine serum and 1% penicillin-streptomycin for 24 hours. The medium was replaced with fresh medium containing 500 μg/ml concentrations of GNPs for 24 hours. These cells were replaced with fresh media and irradiated with 150 kVp photons with 2 mm filter by using X-RAD 320. After irradiations, the cells were incubated for 6 and 24 hours, trypsinized, and centrifuged for both live and dead cells. These cells were collected in RIPA buffer and protease inhibitor at 4 °C for 10 minutes.

Quantified protein lysates were loaded onto NuPAGE™ 12% Bis-Tris gel (Life technology). The gel was subjected to electrophoresis and blotted onto PVDF membrane (0.2μm; Bio-rad, Hercules, CA). Primary antibodies were polyclonal antibodies against Cleaved Caspase-3 (Cell Signaling Technology, Danvers, MA) and monoclonal antibodies against γH2AX (Abcam, Cambridge, MA) and β-actin (MP biomedicals, Eschwege, Germany). Images were acquired by using clear blue X-ray film (CL-X Prosure™ Film; Thermo Fisher Scientific).

2.C. Imaging of Gold Nanoparticles

2.C.a Transmission Electron Microscopy

Cells were plated for 24 h, then exposed to GNPs for another 24 h. Cells were trypsinized, pelleted, and fixed in 2% paraformaldehyde and 2% glutaraldehyde in 0.05 M sodium cacodylate buffer. Cells were postfixed in 1% osmium tetroxide in 0.05 M sodium cacodylate buffer and washed two times with distilled water. En bloc staining was performed overnight with 0.5% uranyl acetate and dehydrated in ethanol, and embedded in agar resin. Sections were cut using an ultramicrotome and stained with 2% uranyl acetate and Reynolds' lead citrate. Prepared samples were observed with JEM-1011 transmission electron microscopy (JEOL, Tokyo, Japan)

2.C.b Optical Diffraction Tomography

Utilizing commercialized optical diffraction tomography (ODT) setups HT-1H (Tomocube, Inc., South Korea), three-dimensional intracellular localization of GNPs inside the cell was quantified by their high refractive index (RI) values. The cells were prepared using the same conditions as for the clonogenic assay before x-ray irradiation.

3. Results

3.A. Radial Dose distribution

The interaction probabilities for the two-photon sources are shown in table 2. The interaction probability depends on both the photon energy and the GNP size. 150 kVp photons have more than a 20% higher interaction probability than 51 keV photons. Increasing the GNP diameter led to an increase in the interaction probability per Gray proportional to the volume, due to the longer path length through the interaction volume for photons.

	2 nm	15 nm	20 nm	50 nm
150 kVp	1.5×10^{-6}	6.1×10^{-4}	1.4×10^{-3}	2.2×10^{-2}
51 keV	1.2×10^{-6}	4.9×10^{-4}	1.2×10^{-3}	1.8×10^{-2}
6 MV	2.9×10^{-7}	1.1×10^{-4}	2.4×10^{-4}	3.5×10^{-3}

Table 5 The interaction probability of GNPs per Gray at 2 cm depth for a range of GNP sizes and for three-photon sources

Figure 16 shows the dose per ionization event for the two-photon sources. As the distance from the single GNP increased, the dose originating from the GNP decreased rapidly. The dose per ionization event in close proximity to the largest GNP was less than that of the smallest GNP. This was likely due to the reabsorption of low-energy electrons created inside the larger GNPs. The dose per ionization event for a 15 nm GNP was up to 10 times larger near the surface compared to a 50 nm GNP. The GNP size dependent dose differences decreased as the distance from the GNP surface increases. Step-like patterns were observed at certain distances. This was due to a large number of low-energy Auger electrons ejected from the GNP by kilovoltage photons as described in our previous study,[32] disabling Auger processes removed these step-like patterns (see Figure 16). For megavoltage photons, however, the step-like patterns were greatly reduced due to smaller contribution from Auger electrons (Figure 16(c)). We found a fitting curve of $Dose = a \cdot (radius)^b + c$ (a, b, and c are parameters fitted for several radial bins). The fit curve is also shown figure 16 for comparison. The default break points between radial ranges were determined by 0.02 (or 0.04), 0.1, 0.2, 1, 2, 10, 20, 30, 40, and 50 μm and few more points were added if necessary. The differences between the analytical fit and the simulation were within 10% for radial distances of < 20 μm.

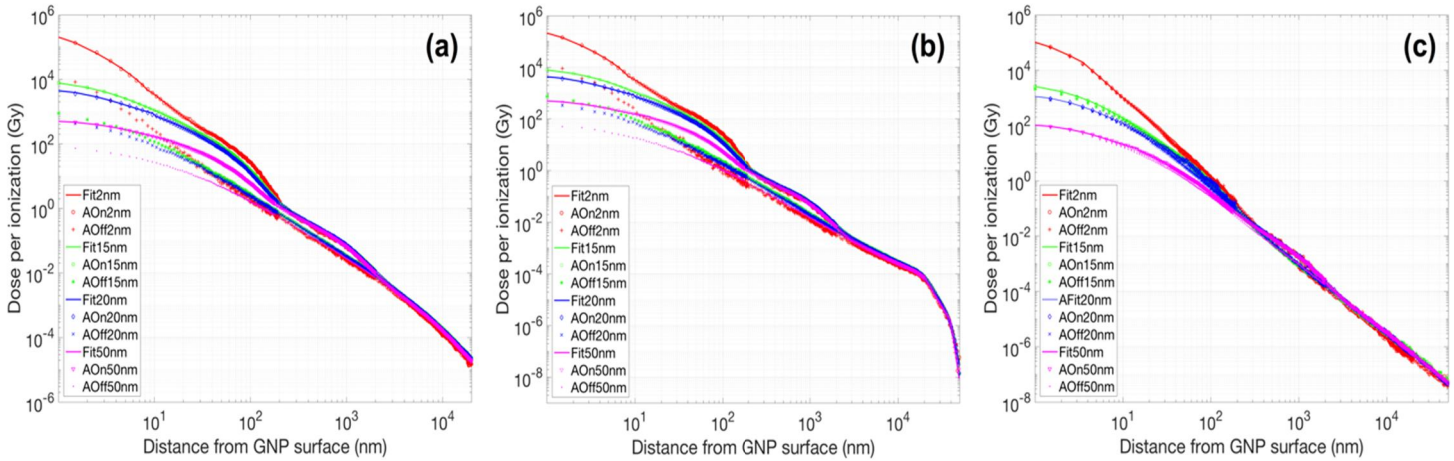

Figure 16 Fitting curve and radial dose distributions as a function of distance from the GNP surface calculated with Monte Carlo for (a) 150 kVp, (b) 51 keV, and (c) 6 MV photon beams (AOn/AOff = with/without Auger electron contributions from atomic de-excitation processes). Results for GNP sizes of 2, 15, 20 and 50 nm are plotted.

3.B. Effect Modeling

3.B.a Case 1 – Cell Shapes

The effect of the cell shape on the radiation dose response was investigated (Figure 17). The eccentricity was calculated to quantify the magnitude of the cell shape change according to Table 3. The amount of radiosensitization enhancement increased from a factor of 1.07 to 1.10 for the smaller cell (i.e., MDA-MB-231). On the other hand, for the large cell (F-98), the shape of the cell did not significantly affect the results when the nucleus was placed in the cell center.

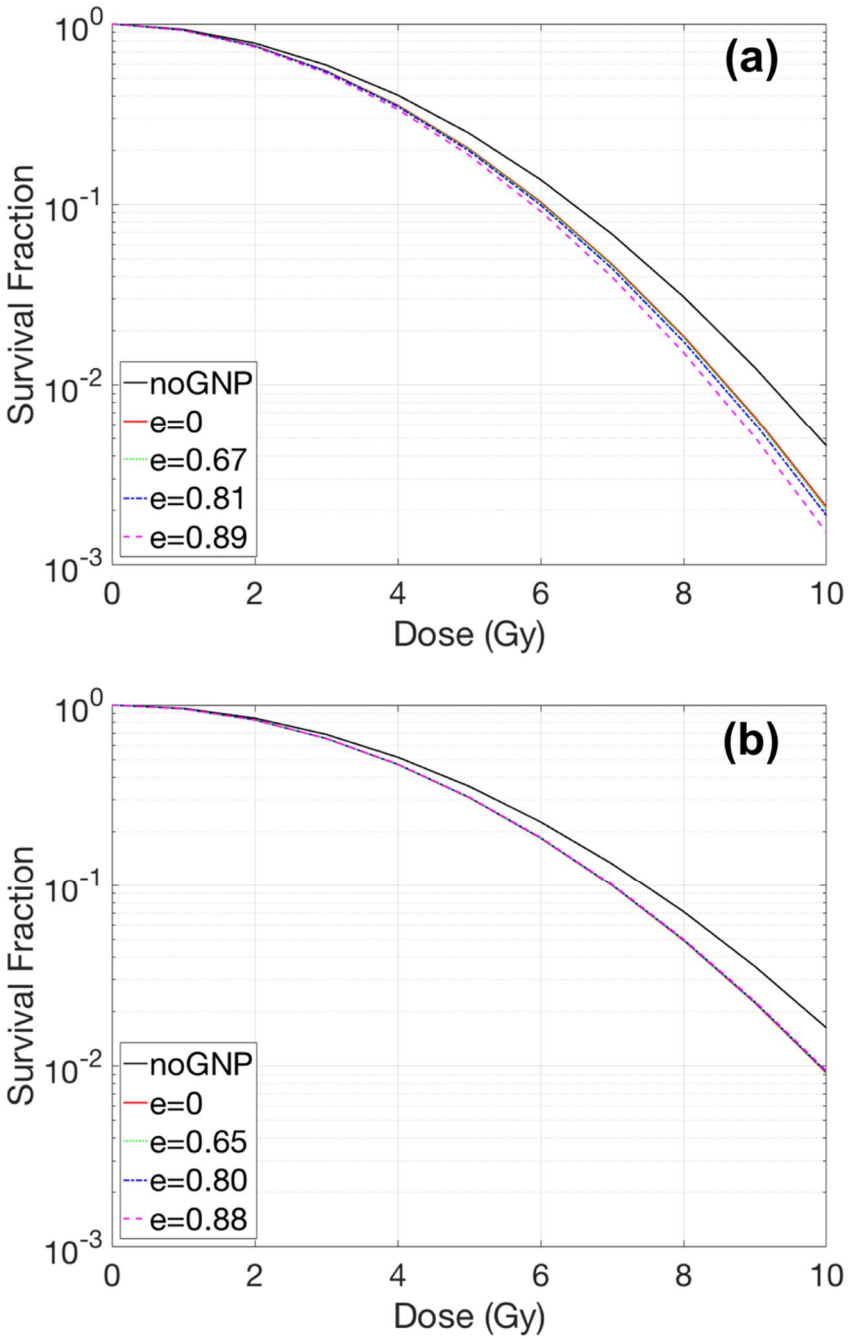

Figure 17 Dose-response curves with various eccentricities for (a) MDA-MB-231 and (b) F-98 cells. GNPs, of 15 nm diameter, were concentrated in media by a 2% weight ratio. Here e = eccentricity, a unitless quantity.

3.B.b Case 2 – Shifted Nucleus

Figure 18 and 19 show the effect of the nucleus location on radiation dose response and its sensitivity enhancements. The shift of the nucleus within the cell was denoted as the distance between the center of the cell and the nucleus divided by the radius of the cell. The GNP radiosensitization depended not only on the cell shape but also on the location of the nucleus. For the circular cell geometries (Figure 18), the SER differed by less than 10% for various distances between the nucleus surface and the cell membrane. The relative SER differences for F-98 were larger than those for MDA-MB-231 cells because the geometric variations for the larger cell were more profound due to its smaller nucleus/cell size ratio. For elliptical cells, the SER was increased up to 1.16 for MDA-MB-231 and 1.22 for F-98. The maximum SER was obtained when the nucleus was located along the major axis.

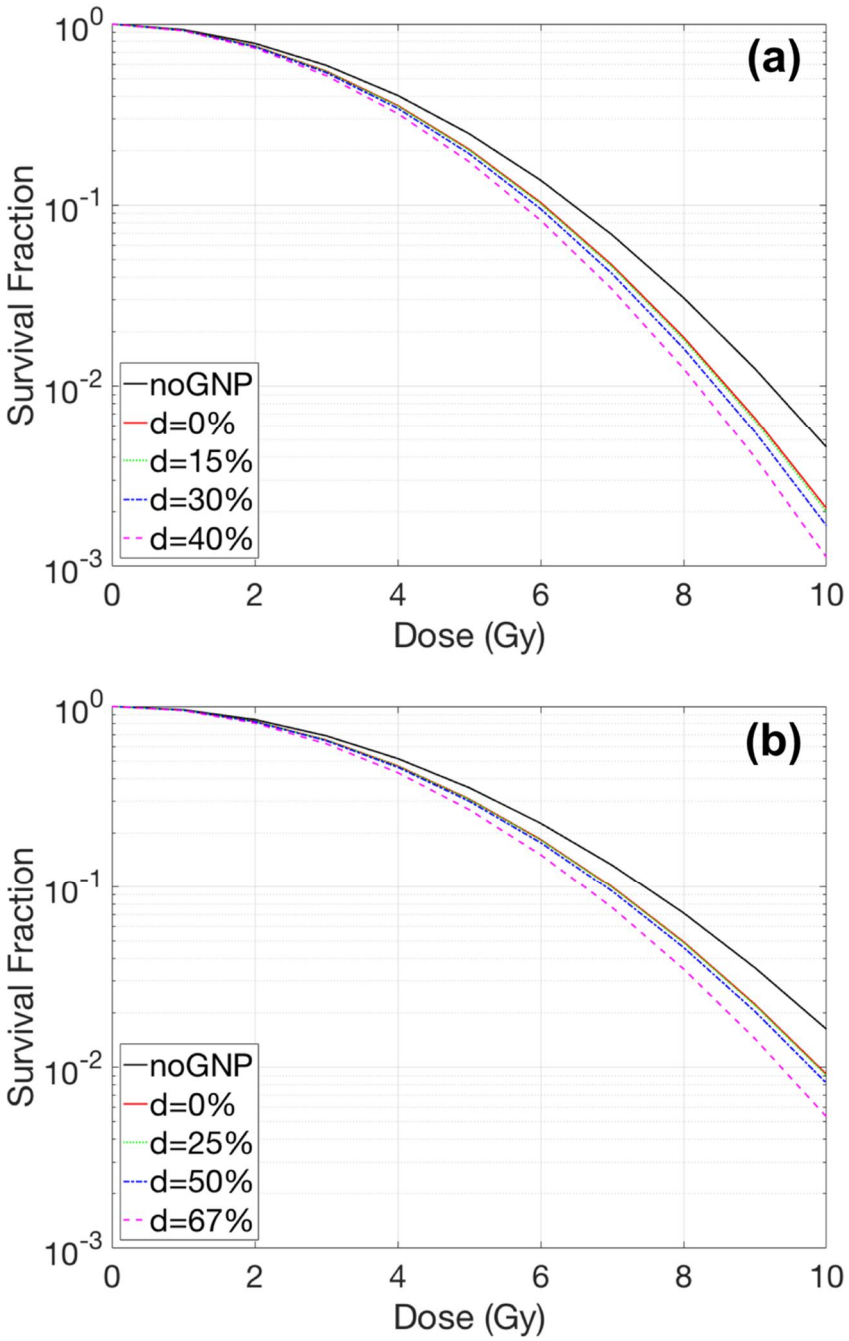

Figure 18 Dose-response curves with various nucleus locations inside a circular cell for (a) MDA-MB-231 and (b) F-98. The GNP with a diameter of 15 nm was concentrated in media by a 2% weight ratio. The parameter d describes the distance between the center of the cell and the center of the nucleus/radius of cell in %.

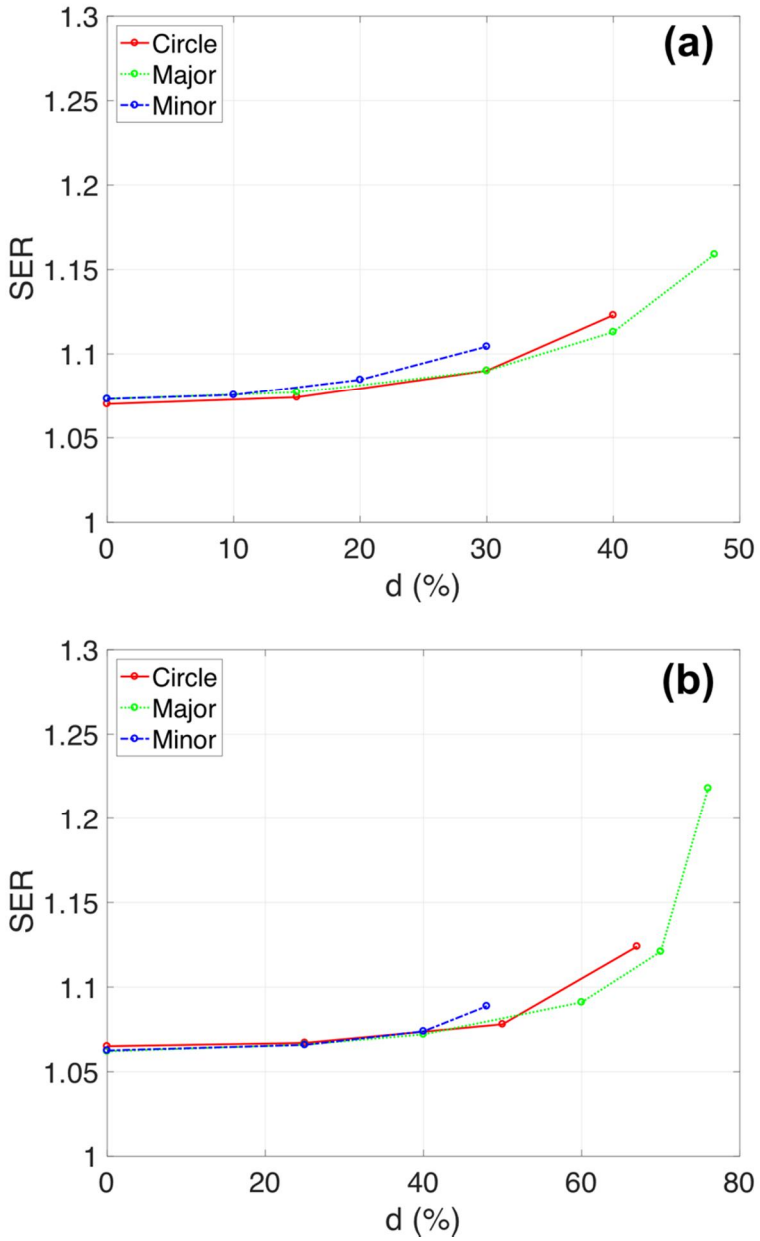

Figure 19 Sensitivity enhancement ratio (SER) versus center between nucleus and cell (=d; the distance between the center of the cell and the center of the nucleus/cell ratio in %) depending on cell shape for (a) MDA-MB-231 and (b) F-98. For elliptical cells, major/minor cell diameters are 15.5/11.5 and 44/20.5 μm for MDA-MB-231 and F-98 cells, respectively. The circular nucleus was located either along the major or the minor axis. The GNPs had a diameter of 15 nm with a concentration in the media of 2% by weight.

The GNP radiosensitization was further quantified inside the nucleus (figure 20, 21, and 22). The nucleus was shifted such that the distance between the cell and nuclear membrane was 50 nm. For the elliptical MDA-MB-231 cells with the nucleus located along the major axis, the MDEF was 1.23 when the sub-region was reduced to half the size of the nucleus and increased up to 1.69 for the smallest size of the sub-region (=0.4 μm) (see figure 20). This MDEF dependency on the size of the sub-region was stronger for the larger size F-98 cells. Additionally, the nucleus located along the major axis could result in a higher MDEF than along the minor axis in elliptical cells because overall the cell membrane and GNPs are closer to the nucleus when it is on the major axis.

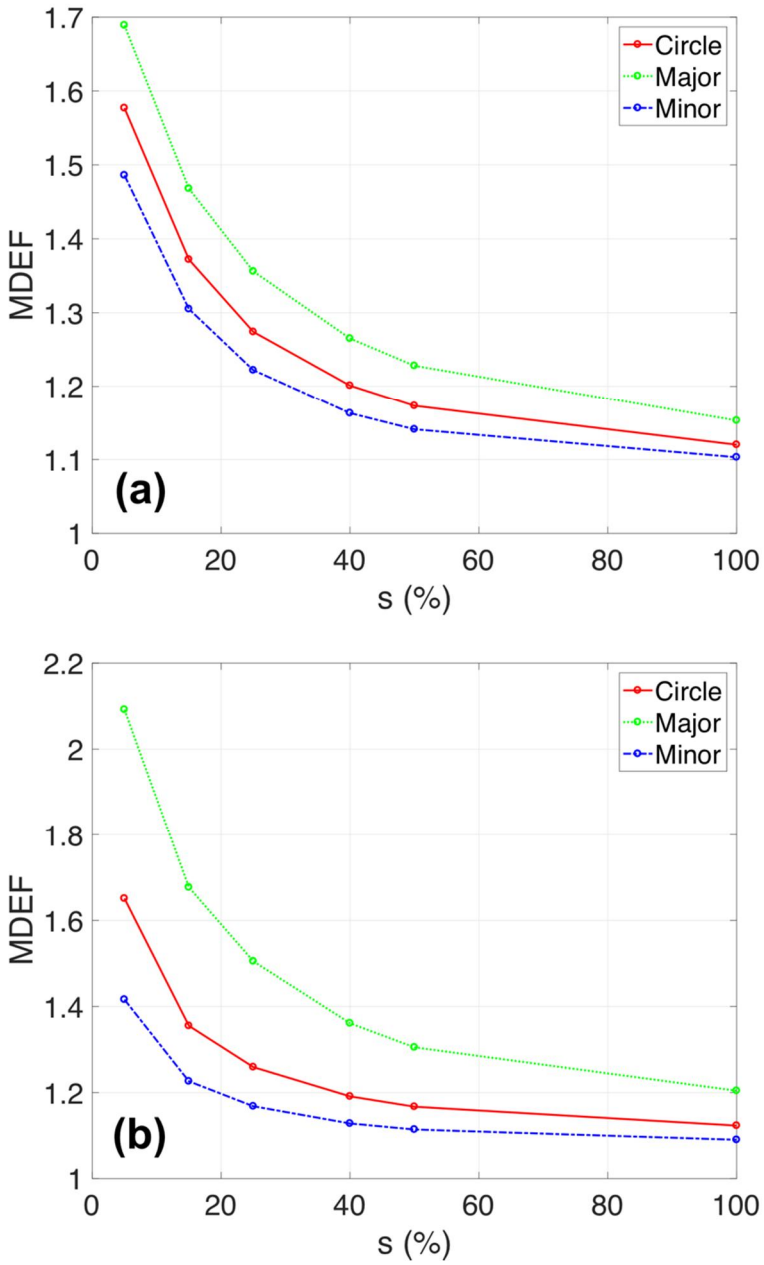

Figure 20 Mean dose enhancement factor (MDEF) versus the size of sub-regions (=s) depending on the cell shape for (a) MDA-MB-231 and (b) F-98. For elliptical cells, major/minor cell diameters are 15.5/11.5 and 44/20.5 μm for MDA-MB-231 and F-98 cells. The circular nucleus was located along major/minor axis and the distance between the cell and the nuclear membrane was 50 nm. The GNPs had a diameter of 15 nm with a concentration in the media of 2% by weight. The percentage refers to the sub-regions per nucleus diameter.

The heat-map of lethal event induction in the nucleus is displayed in figure 21 and 22. The lethal damage distribution in the nucleus varied depending on the size of the cell as well as the location and size of the nucleus within the cell. For elliptical cells, the largest lethal event enhancement was observed when the nucleus was shifted along the major axis due to the large dose enhancement. The lethal event distribution was found to be heterogeneous in the nucleus and closely related to the distance to the GNP-containing medium.

The heterogeneity of dose and lethal event enhancement was due to the nucleus location of the cells. When the nucleus was in the center of the cell, the differences between maximum and minimum MDEF were negligible (< 0.02). The ratios of the standard deviations/mean of lethal event enhancement were subsequently reduced from 0.20 and 0.20 to 0.02 and 5.69e-4 when the nucleus was located in the center of the cell for circular MDA-MB-231 and F-98 cells, respectively.

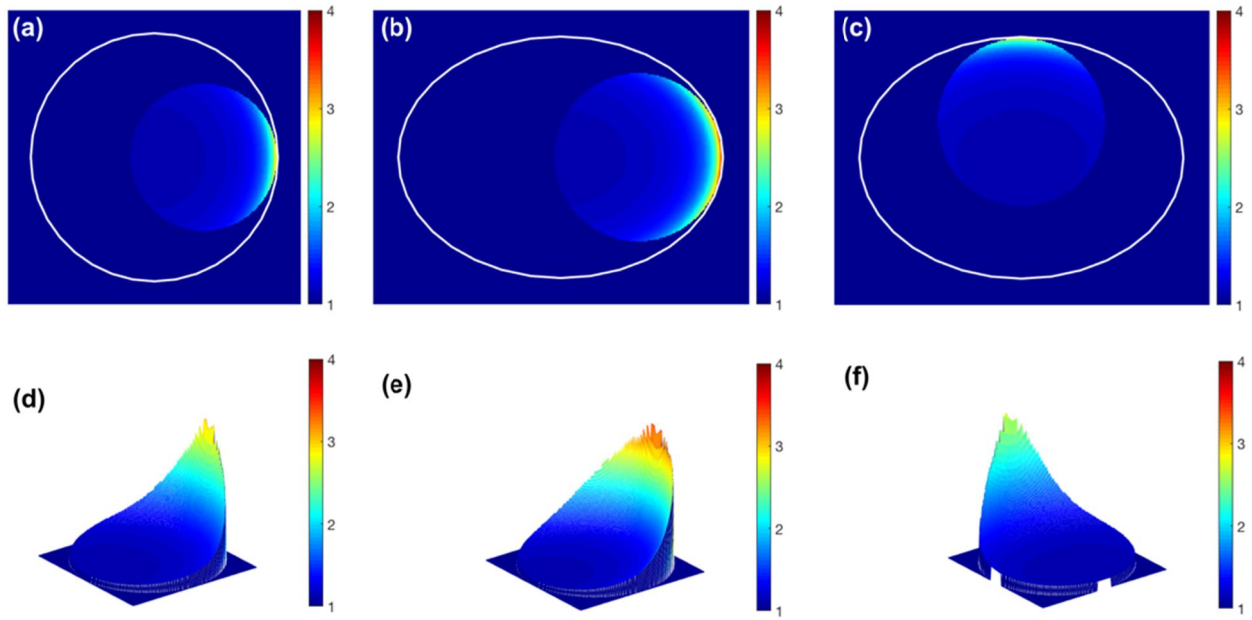

Figure 21 Lethal event enhancement distributions for (a, d) circular and (b, c, e, f) elliptical MDA-MB-231. For elliptical cells, the major/minor axis ratio is 15.5/11.5 μm for MDA-MB-231. The circular nucleus was located along the major/minor axis and the membrane distance between the cell and the nucleus was 50 nm. The GNPs, with diameter of 15 nm, had a concentration in the extracellular media of 2% by weight. The area excluding the nucleus is

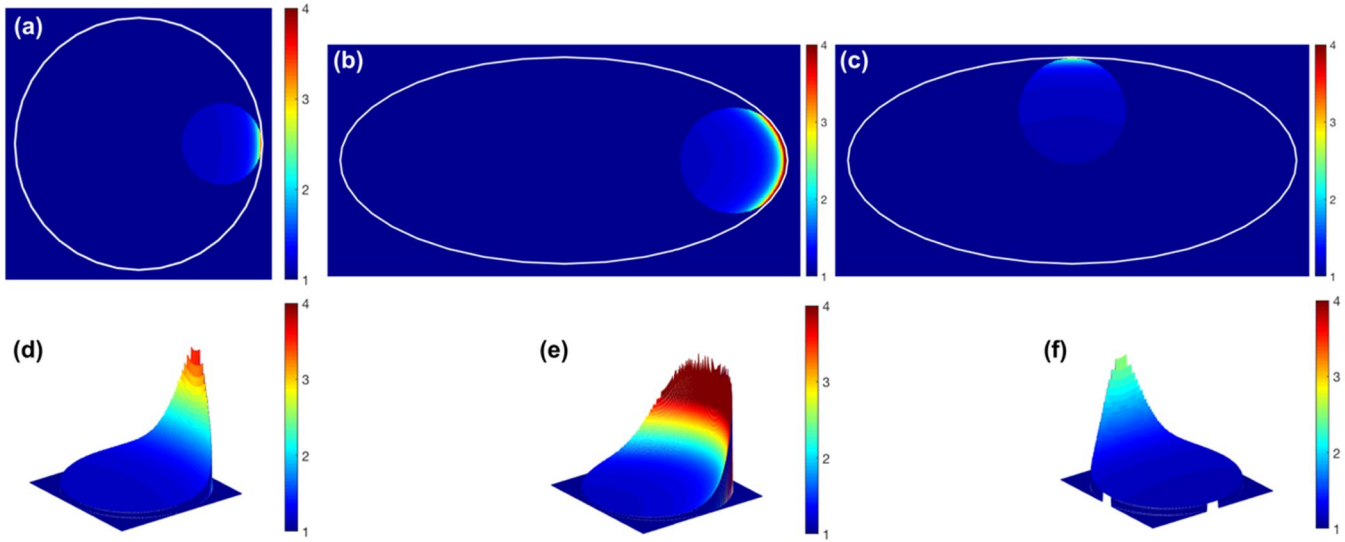

Figure 22 Lethal event enhancement distributions for (a, d) circular and (b, c, e, f) elliptical F-98. For elliptical cells, the major/minor axis ratio is 44/20.5 μm for F-98 cells. The circular nucleus was located along the major/minor axis and membrane distance between cell and nucleus was 50 nm. The GNPs, of diameter 15 nm, had a concentration in the extracellular media of 2% by weight. The area excluding the nucleus is masked as 1.

3.B.c Case 3 – GNP Sizes

For the same concentration of GNPs (mass weight 2%), the size of the GNPs influenced the radiosensitization for both cell lines. Figure 23 shows the results for elliptical cells having a 50 nm gap between the cell and nuclear membrane. As the size of the GNPs is reduced, the SER slightly increases from 1.13 to 1.16 for MDA-MB-231 cells and 1.17 to 1.22 for F-98 cells. Even though smaller GNPs have a higher dose per ionization at their surface, the effect of the GNP size on radiosensitization was limited when the GNPs were located outside the cell with a 50 nm distance between the cell and nuclear membrane. As can be seen in figure 16, the largest difference between the dose distributions from GNPs occurs within the first 50 nm to 100 nm.

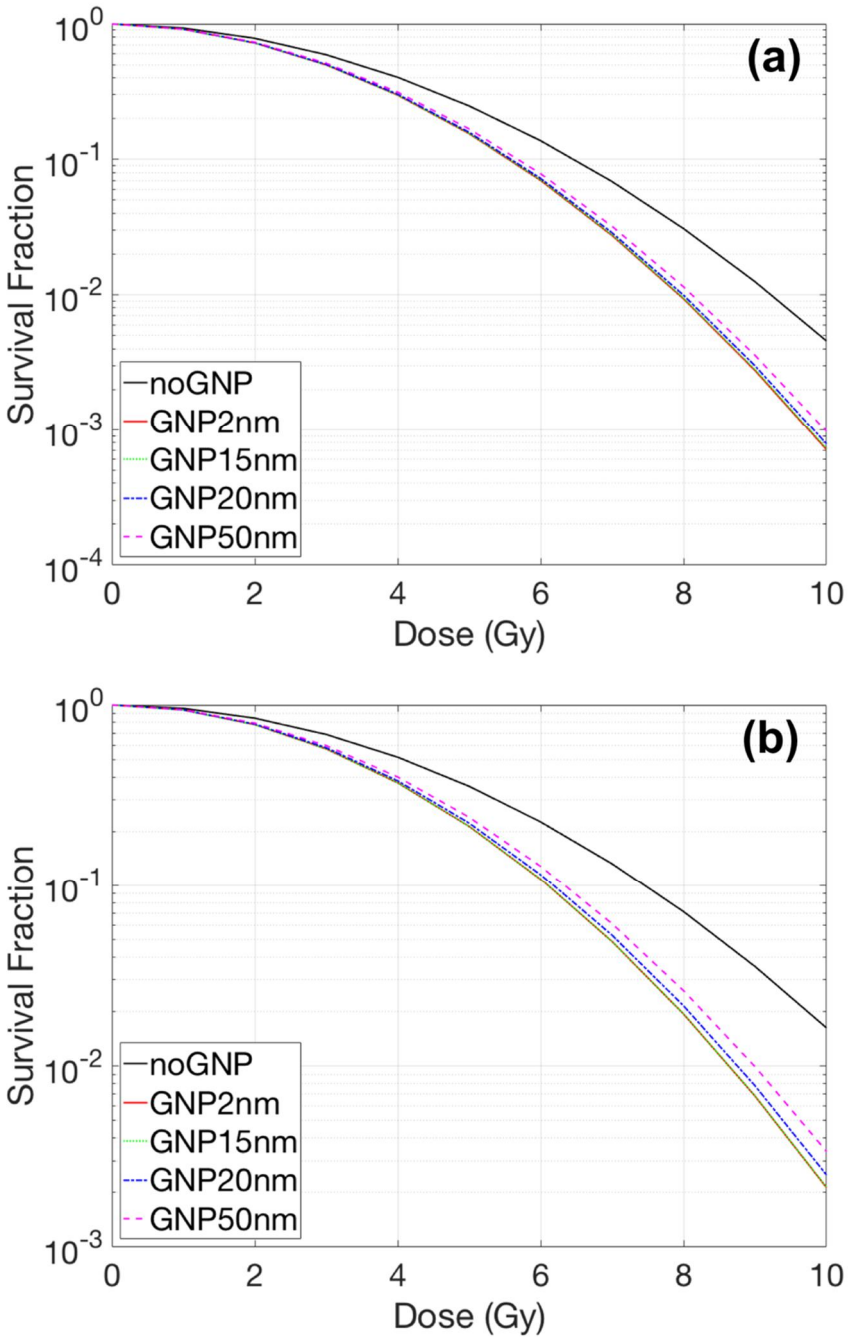

Figure 23 Dose-response curves for various GNP diameters with 150 kVp for an elliptical cell of (a) MDA-MB-231 and (b) F-98. For elliptical cells, the major/minor axis ratio is 15.5/11.5 and 44/20.5 μm for MDA-MB-231 and F-98 respectively. The distance between the cell and nuclear membrane was 50 nm. The GNPs were distributed in the extracellular media with a concentration of 2% by weight.

3.B.d Case 4 – 6 MV Beams

The radiosensitization effects of higher photon energy (6 MV) was investigated for both cell lines with a 2% mass weight concentration of GNPs. However, no GNP radiosensitization was observed for 15 nm GNP and 2% mass weight (Figure 24). Their SER increases were negligible (only up to 1.01) even when the nucleus was located close to the cell membrane. GNP enhancements are typically not expected to be observable without higher concentrations of GNPs in media.

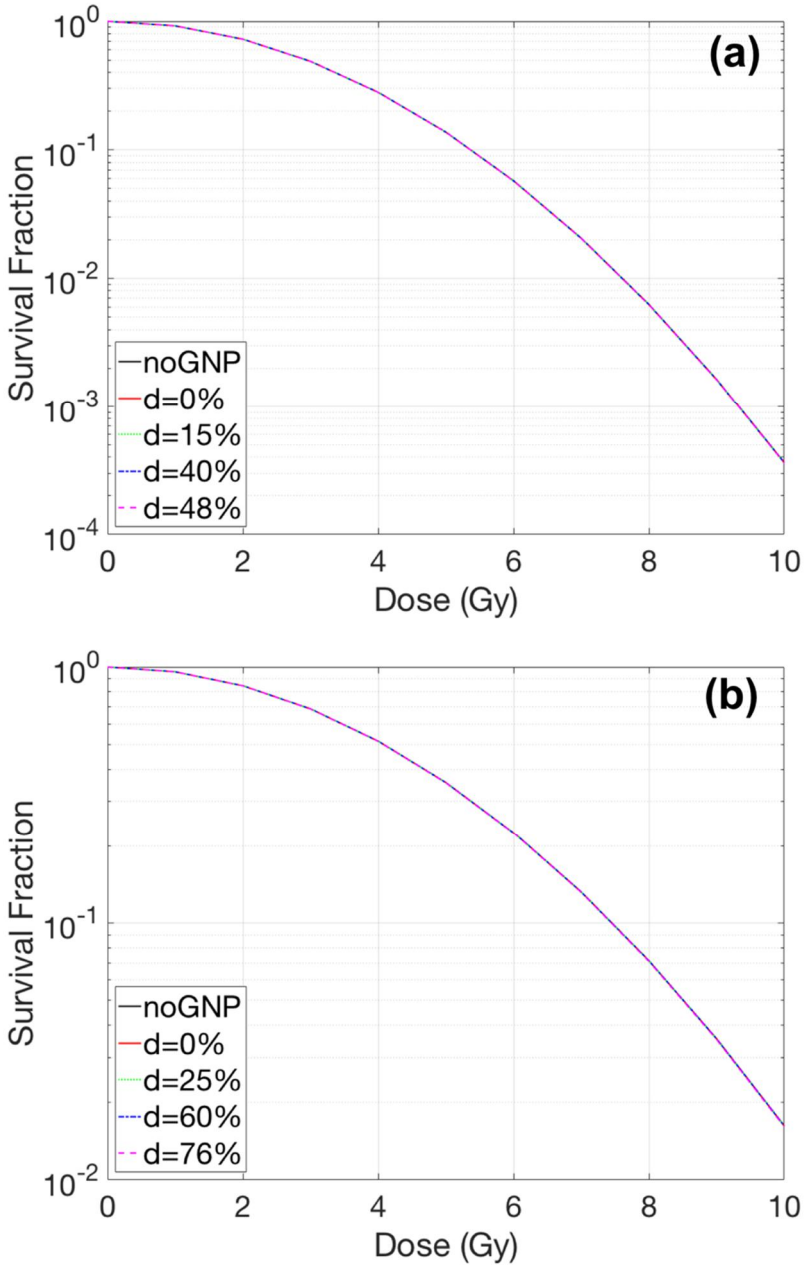

Figure 24 Dose-response curves with 6 MV photon for various nucleus locations inside an elliptical cell of (a) MDA-MB-231 and (b) F-98. For elliptical cells, the major/minor axis ratio is 15.5/11.5 and 44/20.5 μm for MDA-MB-231 and F-98 respectively. The nucleus was located along the major/minor axis and the membrane distance between the cell and the nucleus was 50 nm. The GNP with a diameter of 15 nm was concentrated in media by a 2% weight ratio. The parameter d describes the distance between the center of the cell and the center of the nucleus / radius of cell

in %.

3.C. GNP Uptake and Cellular Toxicity

GNP uptake occurred with concentrations of 1.47 ± 0.02 μg/ml in MDA-MB-231 cells. Number of cells per tube was 6.6 $\times 10^5$ and the volume of the solution is 1 ml per tube. Assuming the number of gold atom per single 1.9 nm diameter GNP is 200, the calculated number of GNPs per cell is 3.40±0.04 $\times 10^7$. Using the clonogenic survival assays, colony formation was reduced by 21%. This is comparable with the 19.4% reduction in previous study.[11] These results indicate that GNPs with 500 μg/ml did not induce remarkable loss of clonogenicitiy on MDA-MB-231 cells.

3.D. Clonogenic Survival Assay

In MDA-MB-231 cells significant radiosensitization occurred at 150 kVp X-rays with a SER of 1.34 (Figure 25). The survival fractions at 6 Gy reduced from 0.0750 for the control group 0.0214 for cells exposed to GNP for 24 h before irradiation. The curve was fitted using simple linear-quadratic model ($Survival\ Fraction = e^{-\alpha D - \beta D^2}$). Their α and β were 0.020 and 0.059, respectively.

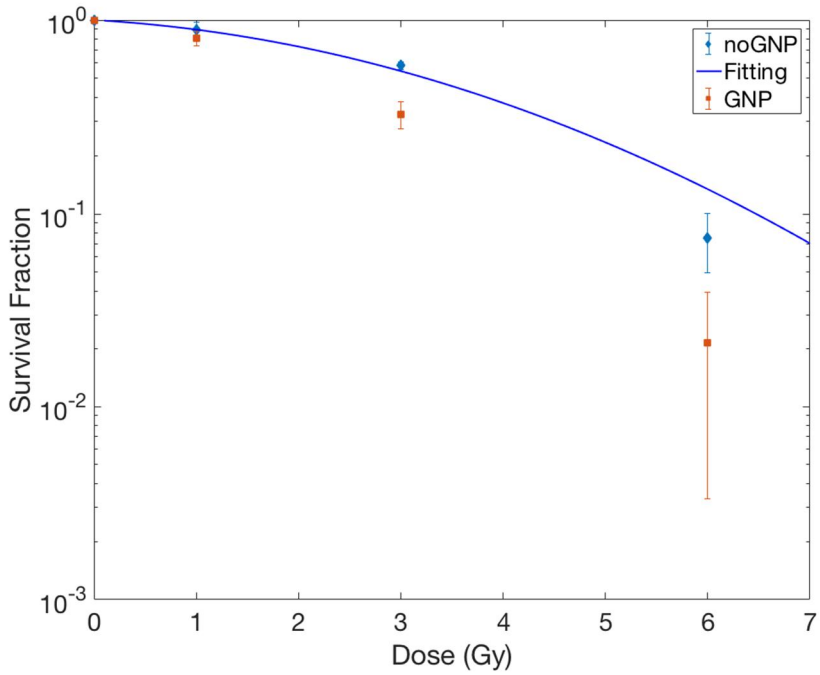

Figure 25 Radiation dose-response curve for MDA-MB-231 cells with gold nanoparticles (GNPs) at 150 kVp photon energies

3.E. Apoptosis and DNA damage

Caspase mediated apoptosis and DNA damage were not measured with cleaved caspase-3 for MDA-MB-231 and 6 Gy irradiation. Other quantification methods such as Annexin-V/PI dual staining or confocal microscope with γH2AX marker are necessary to quantify apoptosis and DNA damage as described in previous studies[79, 80].

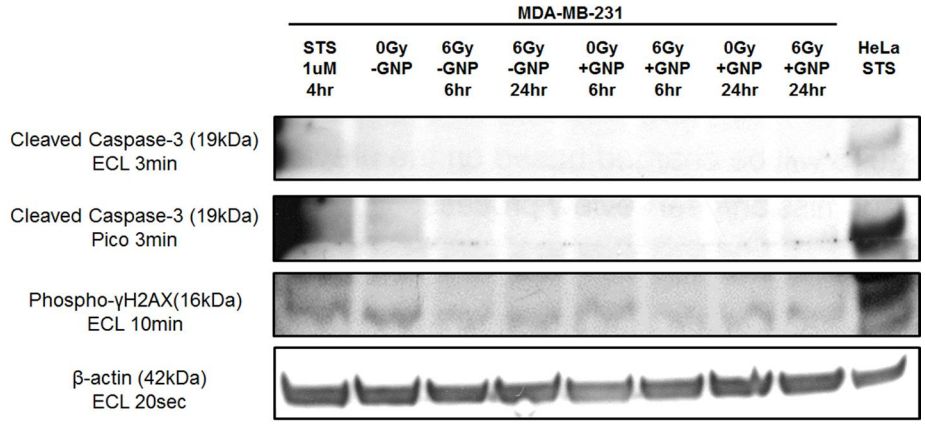

Figure 26 Western blot of proten expressions of cleaved caspase-3, γH2AX and β-actin. Lane 1: positive control with staurosporin (STS); lane 2: negative control without irradiation and gold nanoparticles (GNP) at 24 hr; lane 3: 6 Gy irradiation without GNPs at 6 hr; lane 4: 6 Gy irradiation without GNPs at 24 hr; lane 5: GNPs without irradiation at 6 hr; lane 6: 6 Gy irradiation with GNPs at 6 hr; lane 7: GNPs without irradiation at 24 hr; lane 8: GNPs with 6 Gy irradiation at 24 hr; lane 9: HeLa cell control with STS

3.F. Localization of GNPs

TEM demonstrated that GNPs accumulated in cytoplasmic lysosomes, where they appeared aggregated (Figure 26).

We also observed 3D RI tomograms of GNP-treated and -untreated cells using ODT. To determine the RI values of the GNPs, average RI histograms were compared between GNPs-treated and control cells (Figure 27). For RI values higher than 1.38, a larger number of counts were observed with GNP-treated cells compared to control cells. Since it has been reported that the RI values of the cell cytoplasm were within the range of 1.37- 1.39[81], the regions with RI values higher than usual cytoplasm were assumed to correspond to GNPs.

Intracellular localization of GNPs was assumed based on the regions where RI values were higher than those in the normal cytoplasm (Figure 28). Large amounts of aggregated GNPs in cytoplasmic lysosomes were internalized into the cell within 1-2 h and these aggregated GNPs were dispersed in the cytoplasm as time evolved.

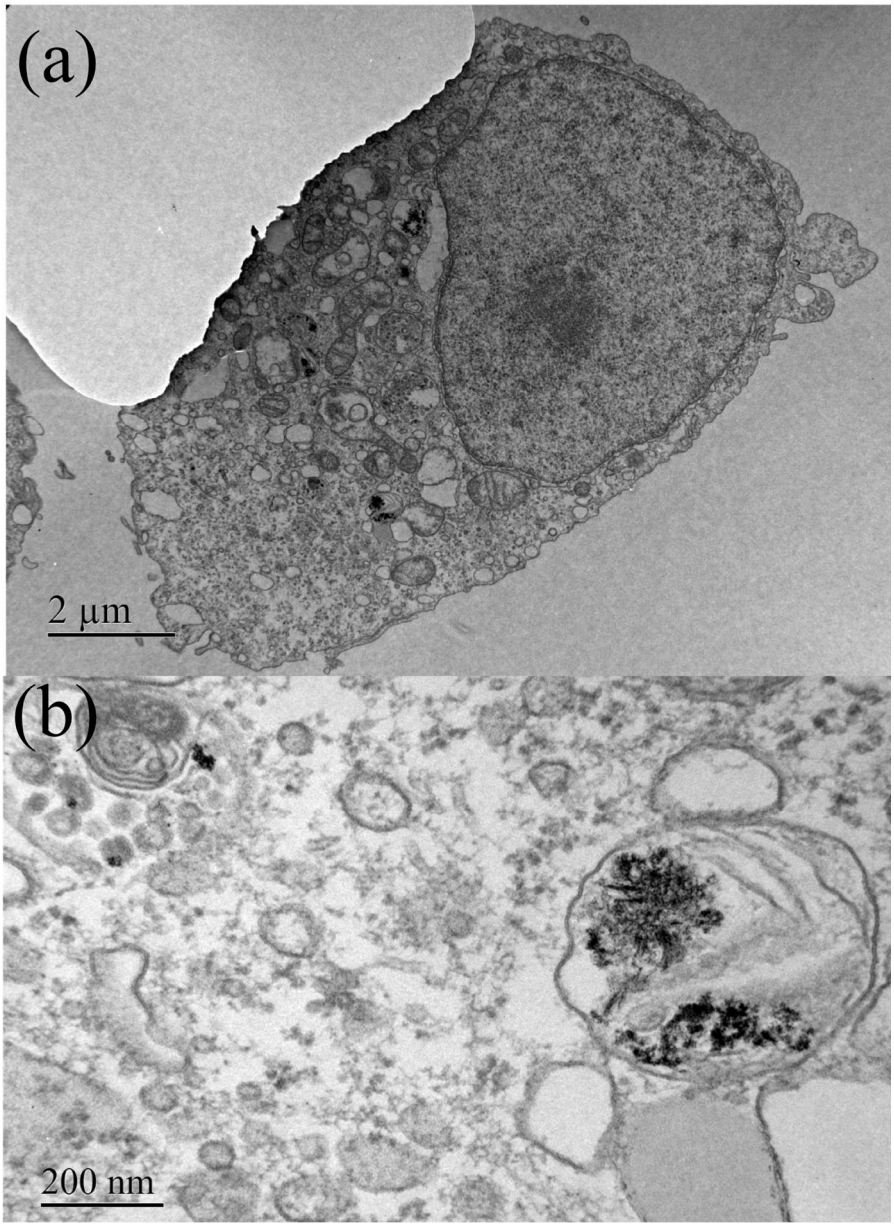

Figure 27 Transmission Electron Microscopy (TEM) images of MDA-MB-231 cell treated with 500 μg/ml of 1.9 nm GNPs. (a) at 2 μm and (b) 200 nm scale

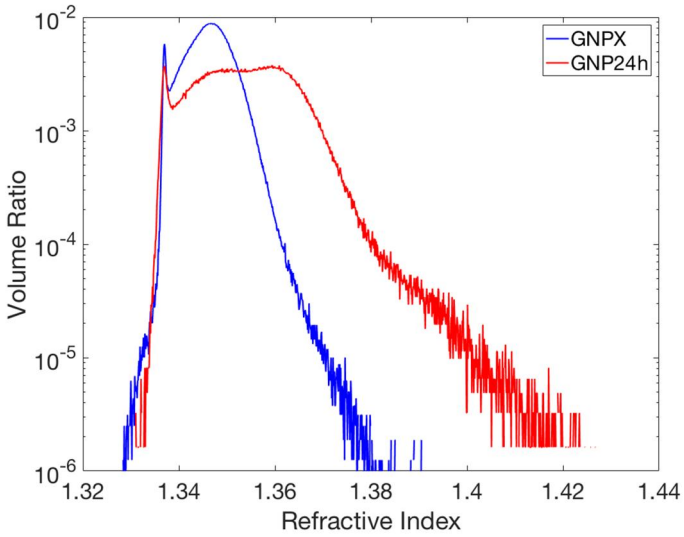

Figure 28 Refractive Index (RI) histogram between without gold nanoparticles (GNPX) and with gold nanoparticles after 24 h (GNP24h)

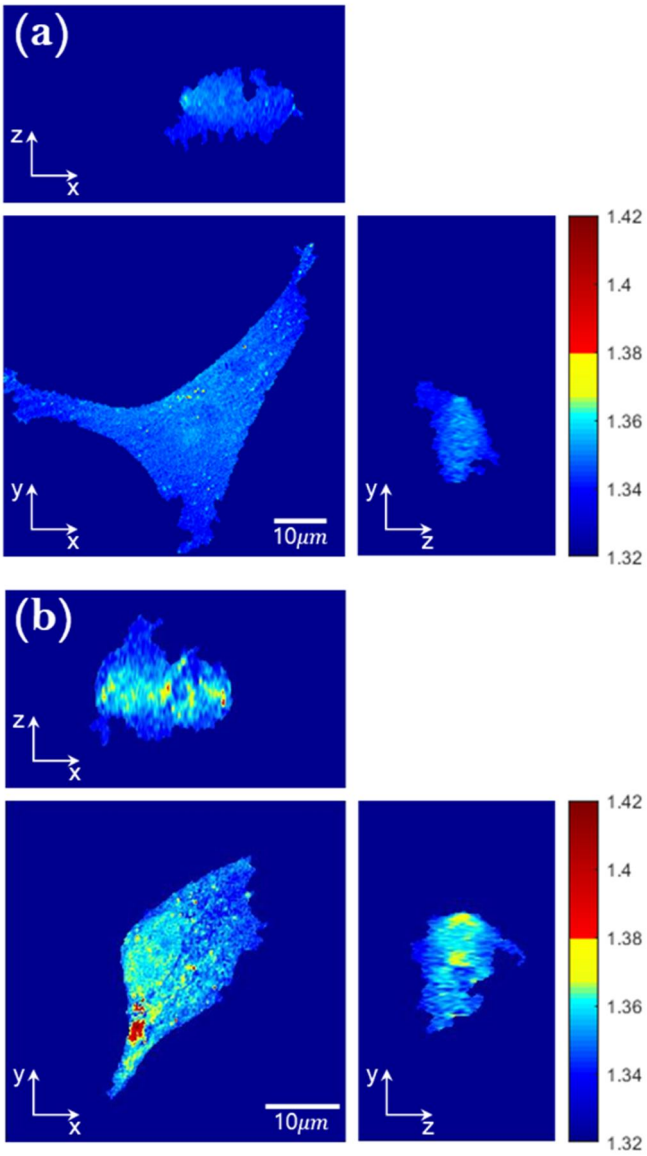

Figure 29 Cross-sectional slices of the 3D RI tomogram of a MDA-MB-231 human breast cancer cell after 24h treatment (a) without and (b) with GNPs. The values on the color bar are corresponding refractive indices.

The distances between GNPs and nucleus membrane was plotted in Figure 29. As reported previously[80], the peak was observed at 0.5 μm outside the nuclear membrane. The number of GNPs decreased rapidly across the nuclear boundary within μm inside the nuclear envelope. Please note that this is the analysis of three-dimensional images.

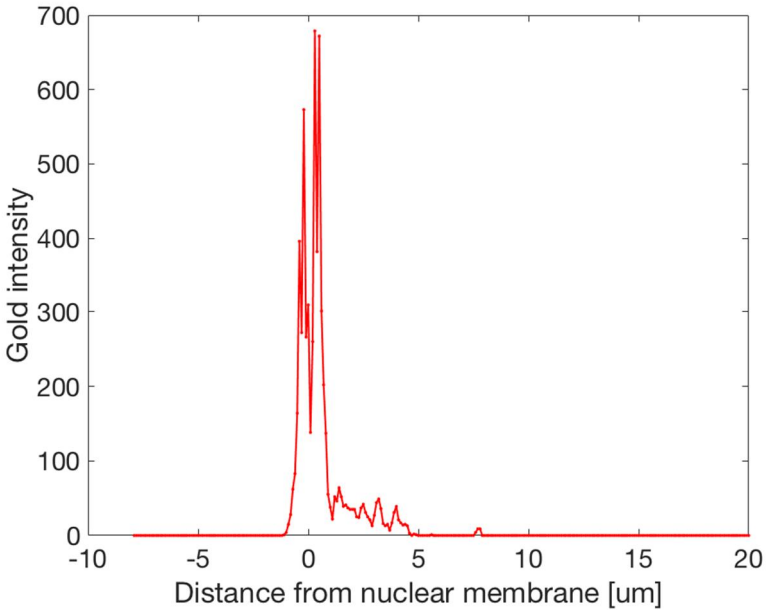

Figure 30 Distance histogram of 1.9 nm Aurovist gold nanoparticles from the nuclear membrane in MDA-MB-231 cells exposed after 24 h.

3.G. GNP Radiosensitization Modeling

The calculated dose distributions fell rapidly off within short distances from the GNPs (<1% of the surface dose at 100 nm). The dose around single a GNP was superimposed at GNP locations (RI>1.38) on the cell geometry at 24 h after GNP treatment. (Figure 30). Cell nucleus was manually identified as lethal events region in GNP-LEM prediction.

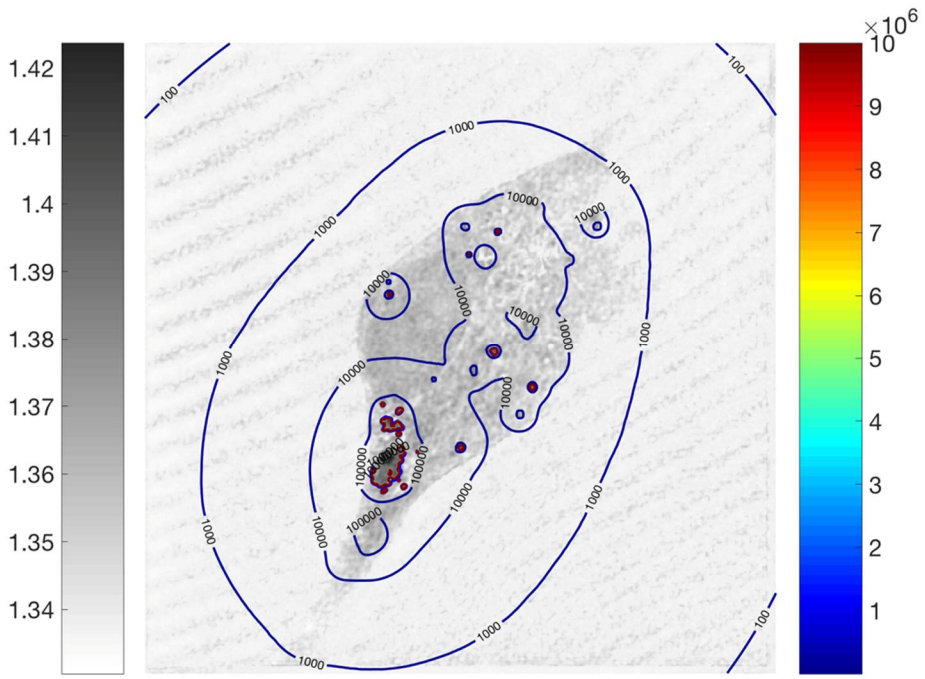

Figure 31 Microscopic dose distributions on cell images acquired by optical diffraction tomography. Grayscale: refractive index, Color scale: microscopic dose (Gy/ionization)

The cell survival fraction was predicted based on GNP-LEM and was compared with experimental results. This agreement is good, substantially better than simple macroscopic physical dose considerations. This suggests that the microscopic dose in the vicinity of GNPs is a significant contribution to experimentally observed GNP dose enhancement. Also, ODT has been successfully shown to provide three dimensional information of cell geometry and GNPs for modeling. (Figure 31).

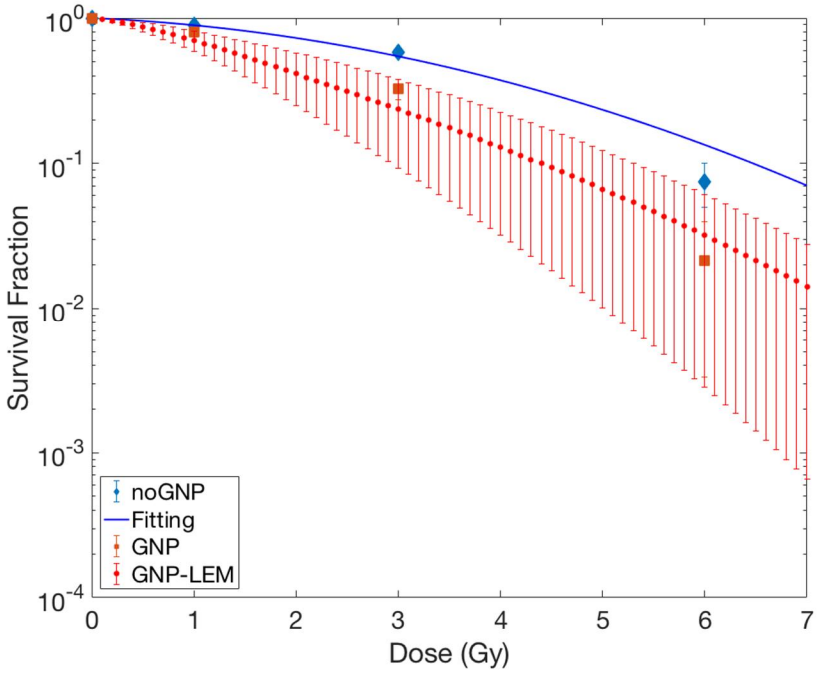

Figure 32 Experimentally observed cell survival for MDA-MD-231 cells exposed to 150 kVp X-rays with (orange square) and without (blue diamond) GNPs. Cell survival fitting without GNPs (blue solid line) and theoretically predicted with GNPs (red circles)

4. Discussion

Detailed modeling of the cell geometries is crucial to better our understanding of GNP radiosensitization. In this paper, we quantified the effects of the cell geometry on GNP radiosensitization using Monte Carlo simulations and a modified Local Effect Model. For the GNP-LEM approach, it is important to not only consider the size and shape of the cell, but also the displacement of the nucleus, and the distribution of GNPs with respect to the cell nucleus, because of the limited range of electrons emitted from the GNPs. We further quantified the dose enhancement in the sub-sections of the nucleus and plotted the lethal event heat maps inside the nucleus to determine the importance of geometrical effects for GNP radiosensitization.

In this study, we only consider the effects of GNPs located in the extracellular media. According to a previous study,[32] if GNPs were able to penetrate the cell and/or nuclear membrane, the GNP mediated dose enhancement in the nucleus would be larger. Additionally, if GNPs are homogeneously distributed in the entire cell region, the effect of varying the cell geometry is expected to be negligible due to the invariance of distances between GNPs and nucleus. Thus, while our approach maximizes the difference of the observed effect when changing the cell geometry, it provides a conservative estimate on the overall GNP mediated radiosensitization. Our study was motivated by the fact that restricting GNPs to the extracellular

medium represents several potential treatment scenarios. GNPs are typically restricted to the extracellular medium for treatment scenarios where GNPs accumulate passively via the EPR effect e.g., vasculature targeted treatments, or in treatments with uncoated (non-targeted) GNPs that do not penetrate tumor cells. Early in vivo studies found an effectiveness of GNPs on tumor cells irradiated only a few minutes after injection.[61] However, in vitro studies have shown that cellular uptake of the NPs takes more than 6 h while a large number of NPs were observed in the extracellular medium before sufficient uptake times.[82]

For this study, we assumed a GNP mass concentration of 2% for the total cell plus the surrounding media. This 2% concentration is relatively high compared to previous in-vitro and in-vivo studies.[6, 11, 61] However, all of the GNPs were located in the media outside of the cell in this study. Hainfeld et al[8] measured a GNP concentration in tumors of 1.5%. Considering that the interstitial fluid for gliomas makes up between 20-40% of the volume, GNP concentrations in the fluid can be as high as 4.5%. The predicted radiosensitization of elliptical F-98 cells with a shifted nucleus increased from 1.16 to 1.22 and 1.53 for GNP concentrations from 1.5% to 2% and 4.5%, respectively.

One limitation of our study is the physics models in the packages used. Geant4-Penelope and Geant4-DNA are incomplete when modeling NPs. For radiation interactions with GNPs, Geant4-Penelope is unable to precisely

reproduce very low-energy electron interactions in the GNP since it is limited to electrons of energies above 100 eV and neglects the reduced dimensionality of the GNPs. This has been shown in work on nanotubes.[30, 49, 50] Furthermore, the interaction probability per Gray with 6 MV photons in this study was found to be higher than that reported in previous studies.[32, 83] We found that this difference was due to the different physics setting used in the two simulations. In this study, we used a lower tracking cutoff, tracking electrons down to an energy of 100 eV, and a lower secondary electron production threshold of 100 eV. These cuts increased the number of low energy events for 6 MV photons because it includes a larger number of (low-energy) electron-gold interactions. In the previous studies,[32, 83] we found that a higher cutoff was necessary for simulating proton irradiations.

The limitations of Geant4-Penelope to model physics interactions only down to 100 eV may result in some approximations/uncertainties of the radial dose in close proximity of the GNPs. Geant4-DNA is able to model the generation of very low-energy electrons (down to ~ few eV), however, it is limited to a liquid water medium and thus cannot be used for interactions with gold within the GNP at this time. The upcoming release of the updated Geant4-DNA physics will further improve the accuracy of radial dose calculations.[47, 48] The latest release of Geant4 (Geant4 v.10.3) features a new Geant4-DNA physics module (option4), which predicts slight differences in the dose as a result of improvements in the Geant4-DNA physics model mainly affecting low-energy electron (e.g., < 100 eV) transportation in water.

Future developments of Geant4-DNA to include physics models for metals would further improve the results of this study in close proximity to GNP.

It is important to note that we performed a theoretical study of the impact of cell geometry in GNP radiosensitization. Radiation therapy is a complex process, which requires quantification of not only the physical dose but also the biochemical reactions such as the generation of free-radicals, DNA repair, and cell cycle disruption. The generation of free-radicals was not considered in this GNP-LEM approach. A number of studies suggest that chemical processes could further amplify GNP mediated radiosensitization.[84] The cellular stress induced by the presence of reactive oxygen species can induce further biological damage. For example, positively charged NPs with an amine functional group were observed to exhibit higher cytotoxicity due to increased intracellular reactive oxygen species. When GNPs are irradiated, they emit electrons. The average remaining charge in a single GNP per ionization event is presented in Table 5. For the same ionization, the remaining charge decreased with increasing GNP size due to a larger number of internally re-absorbed electrons. These charged GNPs have the potential to create additional reactive oxygen species which may cause further damage, in particular, if the GNPs are located inside the cell or the nucleus. Experimental validation is, therefore, necessary to prove the dependency of GNP radiosensitization on cell geometry, including secondary effects.

GNP diameter / Energy	2 nm	15 nm	20 nm	50 nm
150 kVp	4.8	3.4	3.2	2.4
51 keV	5.0	3.6	3.2	2.5
6 MV	1.0	0.3	0.2	0.2

Table 6 The average remaining charge (electron charge) collected in single GNP per ionization at 2 cm depth for four GNP sizes and three-photon sources

In this study, we used a 2D computational model to calculate the biological effect. This 2D assumption is reasonable because most in vitro cell culture studies are performed in near two-dimensional petri dish experiments. The predicted dose in this study is expected to be slightly higher than for a 3D model due to dimension reduction. On the other hand, the additional number of GNPs located above and below the cell in a 3D model may increase the delivered dose to the nucleus. Therefore, absolute values of GNP radiosensitization are likely to be dependent on actual cell geometry in a 3D model. However, this should not affect the conclusions for the trends of cell geometry dependencies.

Another point to notice is that our modeling approach uses alpha/beta ratios determining cell kill using clonogenic assays obtained 9-14 and 11 days after irradiation for MDA-MB-231 and F-98 cells, respectively.[11, 75] Thus, the predicted survival fractions from this study are similar to the cell kill as determined by the number of lethal damages to a cell. A detailed modeling of cell structures (such as DNA bases) with GNPs distributions in 3D in combination with a more mechanistic model of cell repair kinetics and 3D live cell imaging techniques[71, 81] is necessary to distinguish different damage types or endpoints.

In addition to the effect, we quantified the mean dose in certain sub-regions and generated lethal event heat-maps inside the nucleus. The enhancement of dose and lethal events across the nucleus volume was found

to be highly heterogeneous when the nucleus was close to the cell membrane and mostly homogeneous when the nucleus was located at the cell center. The enhancement was mainly limited to small sub-regions in close proximity to the GNPs. Thus, in order to predict radiation response with GNPs, it is important to implement geometries of not only the cell but also the DNA molecules inside the nucleus and the distribution of GNPs in and around the cells. To obtain the biological effects considering the full nuclear deformations and nuclear heterogeneity, one would need to simulate cells and GNPs with full track structure Monte Carlo simulations. Such an approach would further allow us to directly obtain single and double strand breaks of DNA within a realistic DNA representation and model the repair mechanisms mechanistically. The current work was one step along this way.

Previous ODT development study has confirmed that regions having higher RI values (>1.38) represent GNPs by comparing confocal fluorescent images of the same cells with PEGylated GNPs. However, this technique can cause possible errors. As indictaed in previous studies, ODT cannot resolve GNPs from high RI cellular structures such as lipid droplets and carbohydrates. Also, current approaches assumed any pixel with higher RI values was corresponding to the same number of GNPs. It is likely that higher RI values include a larger number of GNPs but this was not assumed in this study due to lack of verification with other imaging techniques. However, average number of GNPs per pixel can still provide the most likely distributions of GNPs and its microscopic dose distributions inside the cell. Moreover, ODT has the

capability to provide temporal evolutions of GNPs before and after irradiations with its fast scanning time for future development.

GNPs may cause cell cycle disruption and enhance radiosensitization because sensitivity of radiation biological effects are dependent on the cell cycle phase. The S-phase cell is the most radioresistant while G2/M phase cell is the most radiosensitive [85]. Several studies showed distinct results of cell phase combining GNPs and radiation. Compared to control, glucose-capped 14-nm GNPs promoted an increase in the G2/M phase of SK-OV-3 cell and enhanced sensitivity to 6 MV x-rays[79]. Roa et al. also reported that 10.8 nm glucose-GNPs alone increase in the G2/M phase in DU-145 cancer cells[86]. However, no significant alterations in cell cycle was observed with 1.9 nm GNPs and MDA-MB-231, which is the same condition with current study[87].

It can be seen that the approach presented in this work predicts sensitizing effects as colony formation after 2 weeks. Even though GNP-LEM provides the macroscopic end point of biological cell survival, it does not provide any mechanistic mechanisms of GNPs radiosensitization from living cell to death. Recent studies suggested that not only the DNA in the nucleus but also another damaged organelle may play a role in cell killing in GNPs radiosensitization [88-90]. One significant extra-nuclear target is the mitochondrion. These organelle are essential for cellular function such as apoptosis regulation, signaling, and reactive species production. Also generation of a larger number of reactive oxygen species on the GNP surface

may cause an elevated level of oxidative stress, which may give damage to cell[87]. However, current approach with three-dimensional live cell imaging and Monte Carlo simulations still offers possible avenues for providing microscopic dose distribution to explain GNPs radiosensitization mechanisms.

5. Conclusions

We performed MC simulations to characterize interactions between GNPs and low-energy photons at the nanometer scale and applied the results to a biological model to quantify the dependency of GNP radiosensitization on the cell geometry. Due to a steep radial dose fall off within short distances from the GNPs (< 1% of the surface dose at 100 nm), geometric parameters such as the shape, size, and location of the cell and the nucleus are important to assess GNP-mediated radiosensitization. If GNPs are not internalized into the cell, the most radiosensitization can be achieved up to 1.22 with lower photon energy for small GNPs, and small squished cells with shifted nucleus. Radiosensitization can be achieved with kV photons even without cellular uptake of GNPs when the nucleus is shifted inside the cell and located in close proximity to the extracellular, GNP-laden region.

Realistic structural properties (cell geometries and distributions of GNPs) could be provided using ODT to give a better understanding on gold nanoparticle radiosensitization.

DISCUSSION

One of the limitations of this study is the physics model used in Monte Carlo calculations. Currently, interactions on an event-by-event basis are implemented only for water in Geant4-DNA. Instead, Geant4-Penelope was used in this study for radiation interactions with metal nanoparticles such as GNPs. It has been reported that this physics model is unable to precisely reproduce very low-energy electron interactions since it is limited to electrons of energies above 100 eV. This may induce some uncertainties on the radial dose in close proximity of the GNPs. Therefore, on-going developments of Geant4-DNA including metal cross sections are highly necessary to improve the results of this study.

Also, the biological modeling in this study has intrinsic weakness. The application of Local Effect Model (LEM) into carbon ion therapy has been successful to predict biological effectiveness accurately. However, application of LEM into nanoparticle-mediated radiosensitization was just the first step to predict its biological effectiveness. Even though LEM has reproduced the results of the clonogenic assay with nanoparticles, this first model does not include radical productions inside the cell and lacks the full track structure information of radiation inside the cell. For a complete understanding of mechanism from nanoparticle to the cell-killing effects, development of mechanistic modeling is necessary based on full track structure simulations and realistic geometry of the cellular structure.

For effective translation of nanoparticle-mediated radiosensitization into the clinical routine, rigorous preclinical studies assisted with physical

approaches are necessary. For in vivo experimental validations, it must be confirmed that the particles with/without PEGylating are nontoxic in certain concentrations. The modeling of nanoparticle-mediated radiosensitization for in vivo clinical setting is also crucial for treatment planning.

CONCLUSIONS

It has been shown that high atomic number metal nanoparticles (especially gold, Z=79) can be applied not only for internal radionuclide therapy but also for external photon therapy. The significant increase in photoelectric interaction probability for metal nanoparticles allows it to increase the microscopic dose. If metal nanoparticles can be preferentially targeted to tumor tissue, this offers one to selectively escalate dose to tumor tissue while sparing nearby sensitive normal tissue.

This study shows that nanometer-scale Monte Carlo calculation framework provides energy spectra and microscopic dose distributions from the addition of nanoparticles to tumors. The biological model was established based on the collected Monte Carlo data under realistic treatment scenarios. The results presented that, for Auger radionuclide therapy, the cellular S-value was increased up to 1.3 when gold nanoparticles are homogeneously distributed inside the cell. Also, for external photon therapy, the results showed that the sensitivity enhancement ratio (SER) was increased up to a factor of 1.2 even without cellular uptake of gold nanoparticles (2% mass weight). Realistic structural properties (cell geometries and distributions of nanoparticles) could be provided with microscopic imaging techniques to develop complete modeling of gold nanoparticle radiosensitization.

REFERENCES

1. Norman A, Adams FH, Riley RF. Cytogenetic effects of contrast media and triiodobenzoic acid derivatives in human lymphocytes. Radiology. 1978;129(1):199-203. doi: 10.1148/129.1.199. PubMed PMID: 693875.
2. Regulla DF, Hieber LB, Seidenbusch M. Physical and biological interface dose effects in tissue due to X-ray-induced release of secondary radiation from metallic gold surfaces. Radiat Res. 1998;150(1):92-100. PubMed PMID: 9650606.
3. Khlebtsov N, Dykman L. Biodistribution and toxicity of engineered gold nanoparticles: a review of in vitro and in vivo studies. Chem Soc Rev. 2011;40(3):1647-71. doi: 10.1039/c0cs00018c. PubMed PMID: 21082078.
4. Cho WS, Cho M, Jeong J, Choi M, Cho HY, Han BS, et al. Acute toxicity and pharmacokinetics of 13 nm-sized PEG-coated gold nanoparticles. Toxicol Appl Pharmacol. 2009;236(1):16-24. doi: 10.1016/j.taap.2008.12.023. PubMed PMID: 19162059.
5. Sabella S, Carney RP, Brunetti V, Malvindi MA, Al-Juffali N, Vecchio G, et al. A general mechanism for intracellular toxicity of metal-containing nanoparticles. Nanoscale. 2014;6(12):7052-61. doi: 10.1039/c4nr01234h. PubMed PMID: 24842463; PubMed Central PMCID: PMCPMC4120234.
6. Hainfeld JF, Slatkin DN, Smilowitz HM. The use of gold nanoparticles to enhance radiotherapy in mice. Phys Med Biol. 2004;49(18):N309-15. PubMed PMID: 15509078.
7. Hainfeld JF, Dilmanian FA, Zhong Z, Slatkin DN, Kalef-Ezra JA, Smilowitz HM. Gold nanoparticles enhance the radiation therapy of a murine squamous cell carcinoma. Phys Med Biol. 2010;55(11):3045-59. doi: 10.1088/0031-9155/55/11/004. PubMed PMID: 20463371.
8. Hainfeld JF, Smilowitz HM, O'Connor MJ, Dilmanian FA, Slatkin DN. Gold nanoparticle imaging and radiotherapy of brain tumors in mice. Nanomedicine (Lond). 2013;8(10):1601-9. doi: 10.2217/nnm.12.165. PubMed PMID: 23265347; PubMed Central PMCID: PMCPMC3657324.
9. Chithrani DB, Jelveh S, Jalali F, van Prooijen M, Allen C, Bristow RG, et al. Gold nanoparticles as radiation sensitizers in cancer therapy. Radiat Res. 2010;173(6):719-28. doi: 10.1667/RR1984.1. PubMed PMID: 20518651.
10. Taggart LE, McMahon SJ, Currell FJ, Prise KM, Butterworth KT. The role of mitochondrial function in gold nanoparticle mediated radiosensitisation. Cancer Nanotechnol. 2014;5(1):5. doi: 10.1186/s12645-014-0005-7. PubMed PMID: 25243023; PubMed Central PMCID: PMCPMC4164854.
11. Jain S, Coulter JA, Hounsell AR, Butterworth KT, McMahon SJ, Hyland WB, et al. Cell-specific radiosensitization by gold nanoparticles at megavoltage radiation energies. Int J Radiat Oncol Biol Phys. 2011;79(2):531-9. doi: 10.1016/j.ijrobp.2010.08.044. PubMed PMID:

21095075; PubMed Central PMCID: PMCPMC3015172.
12. Kong T, Zeng J, Wang X, Yang X, Yang J, McQuarrie S, et al. Enhancement of radiation cytotoxicity in breast-cancer cells by localized attachment of gold nanoparticles. Small. 2008;4(9):1537-43. doi: 10.1002/smll.200700794. PubMed PMID: 18712753.
13. Rahman WN, Bishara N, Ackerly T, He CF, Jackson P, Wong C, et al. Enhancement of radiation effects by gold nanoparticles for superficial radiation therapy. Nanomedicine. 2009;5(2):136-42. PubMed PMID: 19480049.
14. Maeda H, Fang J, Inutsuka T, Kitamoto Y. Vascular permeability enhancement in solid tumor: various factors, mechanisms involved and its implications. Int Immunopharmacol. 2003;3(3):319-28. doi: 10.1016/S1567-5769(02)00271-0. PubMed PMID: 12639809.
15. Hainfeld JF, Slatkin DN, Focella TM, Smilowitz HM. Gold nanoparticles: a new X-ray contrast agent. Br J Radiol. 2006;79(939):248-53. doi: 10.1259/bjr/13169882. PubMed PMID: 16498039.
16. Yang C, Uertz J, Yohan D, Chithrani BD. Peptide modified gold nanoparticles for improved cellular uptake, nuclear transport, and intracellular retention. Nanoscale. 2014;6(20):12026-33. doi: 10.1039/c4nr02535k. PubMed PMID: 25182693.
17. Emfietzoglou D, Papamichael G, Pathak A, Fotopoulos A, Nikjoo H. Monte-Carlo study of energy deposition by heavy charged particles in sub-cellular volumes. Radiat Prot Dosimetry. 2007;126(1-4):457-62. doi: 10.1093/rpd/ncm092. PubMed PMID: 17513851.
18. Bousis C, Emfietzoglou D, Hadjidoukas P, Nikjoo H. Monte Carlo single-cell dosimetry of Auger-electron emitting radionuclides. Phys Med Biol. 2010;55(9):2555-72. doi: 10.1088/0031-9155/55/9/009. PubMed PMID: 20393237.
19. Kassis AI. Cancer therapy with Auger electrons: are we almost there? J Nucl Med. 2003;44(9):1479-81. PubMed PMID: 12960195.
20. Nikjoo H, Emfietzoglou D, Charlton DE. The Auger effect in physical and biological research. Int J Radiat Biol. 2008;84(12):1011-26. doi: 10.1080/09553000802460172. PubMed PMID: 19061125.
21. Paquet F, Barbey P, Bardies M, Biau A, Blanchardon E, Chetioui A, et al. The assessment and management of risks associated with exposures to short-range Auger- and beta-emitting radionuclides. State of the art and proposals for lines of research. J Radiol Prot. 2013;33(1):R1-16. doi: 10.1088/0952-4746/33/1/R1. PubMed PMID: 23296029.
22. Kelkar SS, Reineke TM. Theranostics: combining imaging and therapy. Bioconjug Chem. 2011;22(10):1879-903. doi: 10.1021/bc200151q. PubMed PMID: 21830812.
23. Pronschinske A, Pedevilla P, Murphy CJ, Lewis EA, Lucci FR, Brown G, et al. Enhancement of low-energy electron emission in 2D radioactive films. Nat Mater. 2015;14(9):904-7. doi: 10.1038/nmat4323. PubMed PMID: 26076306.
24. Bernal MA, Bordage MC, Brown JM, Davidkova M, Delage E, El

Bitar Z, et al. Track structure modeling in liquid water: A review of the Geant4-DNA very low energy extension of the Geant4 Monte Carlo simulation toolkit. Phys Med. 2015;31(8):861-74. doi: 10.1016/j.ejmp.2015.10.087. PubMed PMID: 26653251.
25. Nikjoo H, Uehara S. Comparison of various Monte Carlo track structure codes for energetic electrons in gaseous and liquid water. Basic Life Sci. 1994;63:167-84; discussion 84-5. PubMed PMID: 7755542.
26. Howell RW. Radiation spectra for Auger-electron emitting radionuclides: report No. 2 of AAPM Nuclear Medicine Task Group No. 6. Med Phys. 1992;19(6):1371-83. doi: 10.1118/1.596927. PubMed PMID: 1461199.
27. Batič M, Hoff G, Pia MG, Saracco P, Weidenspointner G. Validation of Geant4 simulation of electron energy deposition. IEEE Transactions on Nuclear Science. 2013;60(4):2934-57.
28. Bernal MA, Liendo JA. An investigation on the capabilities of the PENELOPE MC code in nanodosimetry. Med Phys. 2009;36(2):620-5. doi: 10.1118/1.3056457. PubMed PMID: 19292002.
29. Champion C, Incerti S, Perrot Y, Delorme R, Bordage MC, Bardies M, et al. Dose point kernels in liquid water: an intra-comparison between GEANT4-DNA and a variety of Monte Carlo codes. Appl Radiat Isot. 2014;83 Pt B:137-41. doi: 10.1016/j.apradiso.2013.01.037. PubMed PMID: 23478094.
30. Fernández-Varea JM, González-Muñoz G, Galassi ME, Wiklund K, Lind BK, Ahnesjö A, et al. Limitations (and merits) of PENELOPE as a track-structure code. International journal of radiation biology. 2012;88(1-2):66-70.
31. Cho J, Gonzalez-Lepera C, Manohar N, Kerr M, Krishnan S, Cho SH. Quantitative investigation of physical factors contributing to gold nanoparticle-mediated proton dose enhancement. Phys Med Biol. 2016;61(6):2562-81. doi: 10.1088/0031-9155/61/6/2562. PubMed PMID: 26952844.
32. Lin Y, McMahon SJ, Paganetti H, Schuemann J. Biological modeling of gold nanoparticle enhanced radiotherapy for proton therapy. Phys Med Biol. 2015;60(10):4149-68. doi: 10.1088/0031-9155/60/10/4149. PubMed PMID: 25953956.
33. Lin Y, McMahon SJ, Scarpelli M, Paganetti H, Schuemann J. Comparing gold nano-particle enhanced radiotherapy with protons, megavoltage photons and kilovoltage photons: a Monte Carlo simulation. Phys Med Biol. 2014;59(24):7675-89. doi: 10.1088/0031-9155/59/24/7675. PubMed PMID: 25415297.
34. Incerti S, Ivanchenko A, Karamitros M, Mantero A, Moretto P, Tran H, et al. Comparison of GEANT4 very low energy cross section models with experimental data in water. Medical physics. 2010;37(9):4692-708.
35. Sanche L. Cancer treatment: Low-energy electron therapy. Nat Mater. 2015;14(9):861-3. doi: 10.1038/nmat4333. PubMed PMID: 26076307.
36. Skrabalak SE, Chen J, Sun Y, Lu X, Au L, Cobley CM, et al. Gold nanocages: synthesis, properties, and applications. Acc Chem Res.

2008;41(12):1587-95. doi: 10.1021/ar800018v. PubMed PMID: 18570442; PubMed Central PMCID: PMCPMC2645935.
37. Alford R, Ogawa M, Choyke PL, Kobayashi H. Molecular probes for the in vivo imaging of cancer. Mol Biosyst. 2009;5(11):1279-91. doi: 10.1039/b911307j. PubMed PMID: 19823742; PubMed Central PMCID: PMCPMC3407672.
38. Kim YH, Jeon J, Hong SH, Rhim WK, Lee YS, Youn H, et al. Tumor Targeting and Imaging Using Cyclic RGD-PEGylated Gold Nanoparticle Probes with Directly Conjugated Iodine-125. Small. 2011;7(14):2052-60.
39. Ertl H, Feinendegen L, Heiniger H. Iodine-125, a tracer in cell biology: Physical properties and biological aspects. Physics in medicine and biology. 1970;15(3):447.
40. Howell RW, Wessels BW, Loevinger R, Watson EE, Bolch WE, Brill AB, et al. The MIRD perspective 1999. Medical Internal Radiation Dose Committee. J Nucl Med. 1999;40(1):3S-10S. PubMed PMID: 9935082.
41. Meesungnoen J, Jay-Gerin JP, Filali-Mouhim A, Mankhetkorn S. Low-energy electron penetration range in liquid water. Radiat Res. 2002;158(5):657-60. PubMed PMID: 12385644.
42. Plante I, Cucinotta FA. Cross sections for the interactions of 1 eV–100 MeV electrons in liquid water and application to Monte-Carlo simulation of HZE radiation tracks. New Journal of Physics. 2009;11(6):063047.
43. Boudaiffa B, Cloutier P, Hunting D, Huels MA, Sanche L. Resonant formation of DNA strand breaks by low-energy (3 to 20 eV) electrons. Science. 2000;287(5458):1658-60. PubMed PMID: 10698742.
44. Marega R, Karmani L, Flamant L, Nageswaran PG, Valembois V, Masereel B, et al. Antibody-functionalized polymer-coated gold nanoparticles targeting cancer cells: an in vitro and in vivo study. Journal of Materials Chemistry. 2012;22(39):21305-12.
45. Kyriakou I, Emfietzoglou D, Garcia-Molina R, Abril I, Kostarelos K. Electron inelastic mean free paths for carbon nanotubes from optical data. Appl Phys Lett. 2009;94(26). doi: Artn 263113

10.1063/1.3167819. PubMed PMID: WOS:000267697300050.
46. Kyriakou I, Emfietzoglou D, Garcia-Molina R, Abril I, Kostarelos K. Simple model of bulk and surface excitation effects to inelastic scattering in low-energy electron beam irradiation of multi-walled carbon nanotubes. J Appl Phys. 2011;110(5). doi: Artn 054304

10.1063/1.3626460. PubMed PMID: WOS:000294968600115.
47. Kyriakou I, Incerti S, Francis Z. Technical Note: Improvements in geant4 energy-loss model and the effect on low-energy electron transport in liquid water. Med Phys. 2015;42(7):3870-6. doi: 10.1118/1.4921613. PubMed PMID: 26133588.
48. Kyriakou I, Sefl M, Nourry V, Incerti S. The impact of new Geant4-DNA cross section models on electron track structure simulations in liquid water. J Appl Phys. 2016;119(19). doi: Artn 194902

10.1063/1.4950808. PubMed PMID: WOS:000377718100026.
49. Emfietzoglou D, Kyriakou I, Garcia-Molina R, Abril I, Kostarelos K. Analytic expressions for the inelastic scattering and energy loss of electron and proton beams in carbon nanotubes. J Appl Phys. 2010;108(5). doi: Artn 054312

10.1063/1.3463405. PubMed PMID: WOS:000282478900092.
50. Emfietzoglou D, Kyriakou I, Garcia-Molina R, Abril I, Kostarelos K. Quasi first-principles Monte Carlo modeling of energy dissipation by low-energy electron beams in multi-walled carbon nanotube materials. Appl Phys Lett. 2012;100(9). doi: Artn 093113

10.1063/1.3688307. PubMed PMID: WOS:000301504800060.
51. Hartman T, Lundqvist H, Westlin JE, Carlsson J. Radiation doses to the cell nucleus in single cells and cells in micrometastases in targeted therapy with (131)I labeled ligands or antibodies. Int J Radiat Oncol Biol Phys. 2000;46(4):1025-36. PubMed PMID: 10705026.
52. Cornelissen B, Vallis KA. Targeting the nucleus: an overview of Auger-electron radionuclide therapy. Curr Drug Discov Technol. 2010;7(4):263-79. PubMed PMID: 21034408.
53. Antosh MP, Wijesinghe DD, Shrestha S, Lanou R, Huang YH, Hasselbacher T, et al. Enhancement of radiation effect on cancer cells by gold-pHLIP. Proc Natl Acad Sci U S A. 2015;112(17):5372-6. doi: 10.1073/pnas.1501628112. PubMed PMID: 25870296; PubMed Central PMCID: PMCPMC4418858.
54. Violet JA, Farrugia G, Skene C, White J, Lobachevsky P, Martin R. Triple targeting of Auger emitters using octreotate conjugated to a DNA-binding ligand and a nuclear localizing signal. International Journal of Radiation Biology. 2016;92(11):707-15. doi: 10.3109/09553002.2016.1157278. PubMed PMID: WOS:000388629800013.
55. Fang F, Gong PS, Zhao HG, Bi YJ, Zhao G, Gong SL, et al. Mitochondrial Modulation of Apoptosis Induced by Low-dose Radiation in Mouse Testicular Cells. Biomed Environ Sci. 2013;26(10):820-30. doi: 10.3967/bes2013.005. PubMed PMID: WOS:000327021200005.
56. Zhao QL, Kondo T, Noda A, Fujiwara Y. Mitochondrial and intracellular free-calcium regulation of radiation-induced apoptosis in human leukemic cells. International Journal of Radiation Biology. 1999;75(4):493-504. doi: Doi 10.1080/095530099140429. PubMed PMID: WOS:000079745700012.
57. Wang LM, Liu Y, Li W, Jiang XM, Ji YL, Wu XC, et al. Selective Targeting of Gold Nanorods at the Mitochondria of Cancer Cells: Implications for Cancer Therapy. Nano Lett. 2011;11(2):772-80. doi: 10.1021/nl103992v. PubMed PMID: WOS:000287049100078.
58. Kirkby C, Ghasroddashti E. Targeting mitochondria in cancer cells using gold nanoparticle-enhanced radiotherapy: A Monte Carlo study. Medical Physics. 2015;42(2):1119-28. doi: 10.1118/1.4906192. PubMed PMID:

WOS:000349229600057.
59. Matsumura Y, Maeda H. A new concept for macromolecular therapeutics in cancer chemotherapy: mechanism of tumoritropic accumulation of proteins and the antitumor agent smancs. Cancer Res. 1986;46(12 Pt 1):6387-92. PubMed PMID: 2946403.
60. Huff TB, Hansen MN, Zhao Y, Cheng JX, Wei A. Controlling the cellular uptake of gold nanorods. Langmuir. 2007;23(4):1596-9. doi: 10.1021/la062642r. PubMed PMID: 17279633; PubMed Central PMCID: PMCPMC2818780.
61. Hainfeld JF, Dilmanian FA, Slatkin DN, Smilowitz HM. Radiotherapy enhancement with gold nanoparticles. J Pharm Pharmacol. 2008;60(8):977-85. doi: 10.1211/jpp.60.8.0005. PubMed PMID: 18644191.
62. Berbeco RI, Korideck H, Ngwa W, Kumar R, Patel J, Sridhar S, et al. DNA damage enhancement from gold nanoparticles for clinical MV photon beams. Radiat Res. 2012;178(6):604-8. doi: 10.1667/RR3001.1. PubMed PMID: 23148509; PubMed Central PMCID: PMCPMC3525114.
63. McMahon SJ, Paganetti H, Prise KM. Optimising element choice for nanoparticle radiosensitisers. Nanoscale. 2016;8(1):581-9. doi: 10.1039/c5nr07089a. PubMed PMID: 26645621.
64. McMahon SJ, Hyland WB, Muir MF, Coulter JA, Jain S, Butterworth KT, et al. Biological consequences of nanoscale energy deposition near irradiated heavy atom nanoparticles. Sci Rep. 2011;1:18. doi: 10.1038/srep00018. PubMed PMID: 22355537; PubMed Central PMCID: PMCPMC3216506.
65. Jones BL, Krishnan S, Cho SH. Estimation of microscopic dose enhancement factor around gold nanoparticles by Monte Carlo calculations. Med Phys. 2010;37(7):3809-16. doi: 10.1118/1.3455703. PubMed PMID: 20831089.
66. Leung MK, Chow JC, Chithrani BD, Lee MJ, Oms B, Jaffray DA. Irradiation of gold nanoparticles by x-rays: Monte Carlo simulation of dose enhancements and the spatial properties of the secondary electrons production. Med Phys. 2011;38(2):624-31. doi: 10.1118/1.3539623. PubMed PMID: 21452700.
67. Sung W, Jung S, Ye SJ. Evaluation of the microscopic dose enhancement for nanoparticle-enhanced Auger therapy. Phys Med Biol. 2016;61(21):7522-35. doi: 10.1088/0031-9155/61/21/7522. PubMed PMID: 27716643.
68. Martínez-Rovira I, Prezado Y. Evaluation of the local dose enhancement in the combination of proton therapy and nanoparticles. Medical physics. 2015;42(11):6703-10.
69. Bobyk L, Edouard M, Deman P, Vautrin M, Pernet-Gallay K, Delaroche J, et al. Photoactivation of gold nanoparticles for glioma treatment. Nanomedicine: Nanotechnology, Biology and Medicine. 2013;9(7):1089-97.
70. Agostinelli S, Allison J, Amako Ka, Apostolakis J, Araujo H, Arce P, et al. GEANT4—a simulation toolkit. Nuclear instruments and methods in

physics research section A: Accelerators, Spectrometers, Detectors and Associated Equipment. 2003;506(3):250-303.
71. McNamara A, Geng C, Turner R, Mendez JR, Perl J, Held K, et al. Validation of the radiobiology toolkit TOPAS-nBio in simple DNA geometries. Phys Med. 2017;33:207-15. doi: 10.1016/j.ejmp.2016.12.010. PubMed PMID: 28017738; PubMed Central PMCID: PMCPMC5292291.
72. Constantin M, Perl J, LoSasso T, Salop A, Whittum D, Narula A, et al. Modeling the truebeam linac using a CAD to Geant4 geometry implementation: dose and IAEA-compliant phase space calculations. Med Phys. 2011;38(7):4018-24. doi: 10.1118/1.3598439. PubMed PMID: 21858999.
73. Cunningham JE, Jurj AL, Oman L, Stonerock AE, Nitcheva DK, Cupples TE. Is risk of axillary lymph node metastasis associated with proximity of breast cancer to the skin? Breast Cancer Res Treat. 2006;100(3):319-28. doi: 10.1007/s10549-006-9256-2. PubMed PMID: 16823512.
74. Ye SJ, Brezovich IA, Shen S, Kim S. Dose errors due to inhomogeneities in balloon catheter brachytherapy for breast cancer. Int J Radiat Oncol Biol Phys. 2004;60(2):672-7. doi: 10.1016/j.ijrobp.2004.05.039. PubMed PMID: 15380605.
75. Taupin F, Flaender M, Delorme R, Brochard T, Mayol JF, Arnaud J, et al. Gadolinium nanoparticles and contrast agent as radiation sensitizers. Phys Med Biol. 2015;60(11):4449-64. doi: 10.1088/0031-9155/60/11/4449. PubMed PMID: 25988839.
76. Kramer M, Jakel O, Haberer T, Kraft G, Schardt D, Weber U. Treatment planning for heavy-ion radiotherapy: physical beam model and dose optimization. Phys Med Biol. 2000;45(11):3299-317. PubMed PMID: 11098905.
77. Coulter JA, Jain S, Butterworth KT, Taggart LE, Dickson GR, McMahon SJ, et al. Cell type-dependent uptake, localization, and cytotoxicity of 1.9 nm gold nanoparticles. Int J Nanomedicine. 2012;7:2673-85. doi: 10.2147/IJN.S31751. PubMed PMID: 22701316; PubMed Central PMCID: PMCPMC3373299.
78. Kim JK, Seo SJ, Kim HT, Kim KH, Chung MH, Kim KR, et al. Enhanced proton treatment in mouse tumors through proton irradiated nanoradiator effects on metallic nanoparticles. Phys Med Biol. 2012;57(24):8309-23. doi: 10.1088/0031-9155/57/24/8309. PubMed PMID: 23201628.
79. Geng F, Song K, Xing JZ, Yuan C, Yan S, Yang Q, et al. Thio-glucose bound gold nanoparticles enhance radio-cytotoxic targeting of ovarian cancer. Nanotechnology. 2011;22(28):285101. doi: 10.1088/0957-4484/22/28/285101. PubMed PMID: 21654036.
80. McQuaid HN, Muir MF, Taggart LE, McMahon SJ, Coulter JA, Hyland WB, et al. Imaging and radiation effects of gold nanoparticles in tumour cells. Scientific reports. 2016;6:19442.
81. Kim D, Oh N, Kim K, Lee S, Pack CG, Park JH, et al. Label-free

high-resolution 3-D imaging of gold nanoparticles inside live cells using optical diffraction tomography. Methods. 2017. doi: 10.1016/j.ymeth.2017.07.008. PubMed PMID: 28723583.
82. Chithrani BD, Ghazani AA, Chan WC. Determining the size and shape dependence of gold nanoparticle uptake into mammalian cells. Nano Lett. 2006;6(4):662-8. doi: 10.1021/nl052396o. PubMed PMID: 16608261.
83. Lin Y, Paganetti H, McMahon SJ, Schuemann J. Gold nanoparticle induced vasculature damage in radiotherapy: Comparing protons, megavoltage photons, and kilovoltage photons. Med Phys. 2015;42(10):5890-902. doi: 10.1118/1.4929975. PubMed PMID: 26429263; PubMed Central PMCID: PMCPMC4575320.
84. Jain S, Coulter JA, Butterworth KT, Hounsell AR, McMahon SJ, Hyland WB, et al. Gold nanoparticle cellular uptake, toxicity and radiosensitisation in hypoxic conditions. Radiother Oncol. 2014;110(2):342-7. doi: 10.1016/j.radonc.2013.12.013. PubMed PMID: 24444528.
85. Pawlik TM, Keyomarsi K. Role of cell cycle in mediating sensitivity to radiotherapy. Int J Radiat Oncol Biol Phys. 2004;59(4):928-42. doi: 10.1016/j.ijrobp.2004.03.005. PubMed PMID: 15234026.
86. Roa W, Zhang X, Guo L, Shaw A, Hu X, Xiong Y, et al. Gold nanoparticle sensitize radiotherapy of prostate cancer cells by regulation of the cell cycle. Nanotechnology. 2009;20(37):375101. doi: 10.1088/0957-4484/20/37/375101. PubMed PMID: 19706948.
87. Butterworth KT, Coulter JA, Jain S, Forker J, McMahon SJ, Schettino G, et al. Evaluation of cytotoxicity and radiation enhancement using 1.9 nm gold particles: potential application for cancer therapy. Nanotechnology. 2010;21(29):295101. doi: 10.1088/0957-4484/21/29/295101. PubMed PMID: 20601762; PubMed Central PMCID: PMCPMC3016629.
88. McNamara AL, Kam WW, Scales N, McMahon SJ, Bennett JW, Byrne HL, et al. Dose enhancement effects to the nucleus and mitochondria from gold nanoparticles in the cytosol. Phys Med Biol. 2016;61(16):5993-6010. doi: 10.1088/0031-9155/61/16/5993. PubMed PMID: 27435339; PubMed Central PMCID: PMCPMC4993038.
89. Karatas OF, Sezgin E, Aydin O, Culha M. Interaction of gold nanoparticles with mitochondria. Colloids Surf B Biointerfaces. 2009;71(2):315-8. doi: 10.1016/j.colsurfb.2009.02.020. PubMed PMID: 19329288.
90. Ghita M, McMahon SJ, Taggart LE, Butterworth KT, Schettino G, Prise KM. A mechanistic study of gold nanoparticle radiosensitisation using targeted microbeam irradiation. Sci Rep. 2017;7:44752. doi: 10.1038/srep44752. PubMed PMID: 28300190; PubMed Central PMCID: PMCPMC5353761.

Abstract (in Korean)

국 문 초 록

방사선 치료의 목적은 방사선이 전달하는 에너지를 종양에 전달하되 주변 정상 조직에는 피하는 것이다. 세기조절 방사선치료(IMRT)와 같은 첨단 치료전략이 도입되었으나 환자 생존율 향상은 여전히 어렵다. 최근 10 년간 나노입자가 종양에 투여될 경우 방사선 민감도를 증가시킨다는 보고가 이어졌다. 특히 금나노입자(GNP)는 뛰어난 생체적합성을 가지고 있어 관심이 집중되었다. 금속은 큰 원자번호를 가지고 있어 광전효과가 발생할 확률이 크다. 따라서 X 선에 의해 발생하는 2 차 전자가 많아져 암세포에 더 많은 에너지를 전달하는 것으로 생각하였다. 그러나, 거시적 관점에서 필요하다고 계산된 나노입자의 농도보다 더 적은 양에서도 방사선 민감도 증가 효과가 관찰되었다.

본 학위논문은 나노입자가 세포 내에 불균일한 선량분포를 만들고, 이것이 어떤 생물학적 효과를 일으키는지 확인하였다. 첫째로, 나노입자와 동위원소를 결합해 약을 만들어 환자 내부에서 종양에 에너지를 전달하는 “나노입자 오제치료”의 가능성을 분석하였다. 몬테카를로 (Monte Carlo) 시뮬레이션을 이용해 전자 에너지 스펙트럼, 미세 선량 분포, 생물학적 효과를 계산하였다. 둘째로, 나노입자 외부 광자선 치료의 생물학적 효과를 확인하였다. 실제 세포 이미지에 기반한 GNP – 세포 모델을 개발하였다. GNP 에

의한 선량당 세포 생존율이 실험을 통해 측정되고 개발된 모델과 비교되었다. 3 차원 홀로그래픽 현미경을 이용해 세포 내 구조와 GNP 의 분포를 측정하고 이를 통해 실제적인 3D 모델을 개발하였다.

본 연구를 통해, 몬테카를로 시뮬레이션을 이용하여 GNP – 방사선이 나노미터 단위에서 어떤 상호작용을 하는지 밝혔고, GNP 방사선치료효과를 정량화할 수 있는 생물학적 모델을 정립하였다. GNP 주변에 짧은 거리에만 방사선량이 전달되기 때문에 (100 nm 거리에서 표면 방사선량에 비해 1% 이하로 감소), 세포와 GNP 의 모양, 크기, 위치는 GNP 증강 방사선치료를 설명할 때 중요한 요소로 밝혀졌다. 3 차원 현미경을 통해 얻어진 이와 같은 정보는 모델링에 반영되었다. In-vitro 세포 실험을 통해 모델이 올바르게 설정된 것을 검증하였다.

주요어: 방사선치료, 나노입자, 몬테카를로 시뮬레이션, 방사선 감수성 증강 물질, 생물학적 모델링

학 번: 2013-30737